Downloaded from orbit.dtu.dk on: Apr 26, 2024

DTU Library

Heat transfer of a shell and tube sodium acetate trihydrate heat storage tank

Chen, Shan; Yu, Chang; Wang, Gang; Kong, Weiqiang; Tian, Zhiyong; Fan, Jianhua

Published in:
Journal of Energy Storage

Link to article, DOI:
10.1016/j.est.2022.105600

Publication date:
2022

Document Version
Publisher's PDF, also known as Version of record

Link back to DTU Orbit

Citation (APA):
Chen, S., Yu, C., Wang, G., Kong, W., Tian, Z., & Fan, J. (2022). Heat transfer of a shell and tube sodium acetate trihydrate heat storage tank. *Journal of Energy Storage*, *55*, Article 105600. https://doi.org/10.1016/j.est.2022.105600

General rights
Copyright and moral rights for the publications made accessible in the public portal are retained by the authors and/or other copyright owners and it is a condition of accessing publications that users recognise and abide by the legal requirements associated with these rights.

- Users may download and print one copy of any publication from the public portal for the purpose of private study or research.
- You may not further distribute the material or use it for any profit-making activity or commercial gain
- You may freely distribute the URL identifying the publication in the public portal

If you believe that this document breaches copyright please contact us providing details, and we will remove access to the work immediately and investigate your claim.

Journal of Energy Storage 55 (2022) 105600

Contents lists available at ScienceDirect

Journal of Energy Storage

journal homepage: www.elsevier.com/locate/est

Research Papers

Heat transfer of a shell and tube sodium acetate trihydrate heat storage tank

Shan Chen [a], Chang Yu [b], Gang Wang [a], Weiqiang Kong [a], Zhiyong Tian [c], Jianhua Fan [a,*]

[a] Department of Civil and Mechanical Engineering, Technical University of Denmark, Brovej 118, 2800 Kgs. Lyngby, Denmark
[b] School of Environment and Natural Resource, Renmin University of China, Beijing 100872, China
[c] School of Environmental Science and Engineering, Huazhong University of Science and Technology, Wuhan 430074, China

ARTICLE INFO

Keywords:
Supercooled
Sodium acetate trihydrate
Shell and tube
Flexible heat storage
Multiphase model
Measurement

ABSTRACT

Heat storage is the key factor in future energy systems with a large share of renewable energies. A shell and tube heat storage tank capable of both long and short term heat storage has been developed by utilizing stable supercooling of sodium acetate trihydrate. Theoretical and experimental investigations were carried out to determine power, heat exchange capacity rate (HXCR), and stored energy of the heat storage tank during the charge and discharge. Theoretically, a multiphase computational fluid dynamics (CFD) model of the storage was developed. The CFD model was validated against the measurement. The heat transfer mechanisms of the heat storage were investigated. The results show that the multiphase model can satisfactorily predict thermal behaviour of the heat storage under different operation conditions. The CFD model shows that 21.15 kWh of heat was charged into the heat storage unit within 7.5 h, compared to 21.16 ± 0.85 kWh in the measurement. During discharge, 14.05 kWh of sensible heat was discharged as short term heat storage, and 7.65 kWh of latent heat can be released on-demand as long term heat storage. The measured sensible heat and latent heat during discharge are 13.57 ± 0.54 kWh and 7.56 ± 0.30 kWh, respectively, corresponding to a relative difference of 1.2–3.7 % compared to the CFD model. There is a strong natural convection flow in some of the tubes, which significantly increases the heat transfer rate. The energy-weighted heat exchange capacity rates are 850 W/K and 795 W/K during charge and discharge of the heat storage, respectively. The findings of the paper give a good reference for designers and manufacturers of latent heat/cold storage.

1. Introduction

The climate conditions of the Earth were stable during the past 10 thousand years after the ice age; however, a rapid shift in climate conditions occurred over the past few decades, dominantly caused by human activities that are indicated by anthropogenic CO_2 emissions [1]. Besides, humankind reaches the present level of progress and living standards due to the intense use of fossil fuels. Furthermore, fossil fuel accounts for approximately 85 % of the world's energy supply, and fossil energy supplies (coal for approx. 200 years; crude oil for approx. 80 years [2]; natural gas for approx. 210 years [3]) are limited. Additionally, global primary energy demand is projected to peak in the 2020s according to the implications of World Energy scenarios 2019 [4]. Therefore, sustainable energy is promising and investigated in this situation. Among all renewable energies, the growth of solar energy was the highest during the last decade. Solar energy is a virtually inexhaustible and the most abundant energy source, although with drawbacks such as unavailability during night time and reduction of energy production during stormy or rainy weather [5].

Heat storage is perceived as the crucial component in solar heating systems to reduce the time or rate mismatch between supply and demand and enhance the fraction of solar energy use [6]. Heat storage can be classified into two categories based on the storage temperature: high and low temperatures [7]. In high temperature solar thermal energy storage systems, high heat storage density, excellent heat transfer rate, and good long term durability are three essential factors to ensure the technical feasibility of the storage system for solar power generation [8]. In residential buildings, research focuses on heat storage for low-temperature applications, for example, for domestic hot water service, space heating and cooling of buildings, peak load shifting, solar heating applications, and seasonal heat storage [7].

* Corresponding author.
E-mail address: jifa@dtu.dk (J. Fan).

https://doi.org/10.1016/j.est.2022.105600
Received 17 May 2022; Received in revised form 11 August 2022; Accepted 1 September 2022
2352-152X/© 2022 The Authors. Published by Elsevier Ltd. This is an open access article under the CC BY license (http://creativecommons.org/licenses/by/4.0/).

Nomenclature

c_p	Specific heat [J/(kg·K)]
$c_{p,\ water}$	Specific heat of water [J/(kg·K)]
E_k	Internal energy of phase k [J]
F	Heat flux [W]
$\vec{F}$	Body force [N]
$\vec{g}$	Gravity [m/s^2]
G_l	Liquidus Gibbs free energy [J]
G_s	Solidus Gibbs free energy [J]
h_{conv}	Heat convection coefficient [W/(m^2·K)]
$h_{j,\ k}$	Enthalpy of species j in phase k [J/kg]
H_l	Enthalpy of liquid phase [J/kg]
H_s	Enthalpy of solid phase [J/kg]
H_m	Heat of fusion [J/kg]
$\vec{J}_{j,k}$	Diffusive flux of species j in phase k [kg/(m^2·s)]
k_{eff}	Effective thermal conductivity [W/(m·K)]
$\dot{m}_{kp}$	Mass from phase k to p [kg/(m^3·s)]
$\dot{m}_{pk}$	Mass from phase p to k [kg/(m^3·s)]
$\dot{m}_{ls}$	Mass from liquid to solid phase [kg/(m^3·s)]
$\dot{m}_{sl}$	Mass from solid to liquid phase [kg/(m^3·s)]
p	Pressure [Pa]
P	Power of the storage unit [W]
P_{loss}	Heat loss rate of the storage unit [W]
S_h	Volumetric heat sources [W/m^3]
S	Surface area [m^2]
S_l	Entropy of liquid phase [J/(kg·K)]
S_s	Entropy of solid phase [J/(kg·K)]
t	time [s]
t_a	Elapsed time during charge [s]
t_b	Elapsed time during discharge [s]
t_0	Trigger time point [s]
T	Temperature [K]
T_a	Ambient temperature [K]
T_i	Temperature before grid adaption [K]
T_i'	Temperature after grid adaption [K]
T_{in}	Water inlet temperature [K]
T_m	Melting temperature [K]
T_{out}	Water outlet temperature [K]
T_{htf}	Temperature of HTF [K]
T_{sto}	Temperature of PCM region [K]
$\dot{V}water$	Volume flow rate [L/min]
α_k	Volume fraction of phase k [–]
α_l	Volume fraction of liquid phase [–]
α_s	Volume fraction of solid phase [–]
ΔG_k	Gibbs free energy of homogeneous nucleation [J]
$\Delta G_k{}'$	Gibbs free energy of heterogeneous nucleation [J]
ΔG_s	Surface energy [J]
ΔG_v	Volumetric energy [J]
ΔG_{vv}	Volumetric energy [J/m^3]
ΔH	Enthalpy difference [J/kg]
ΔS	Entropy difference [J//(kg·K)]
ΔT	Temperature difference [K]
Δt	Time interval [s]
μ_m	Viscosity of the mixture [Pa·s]
$\vec{\nu}_{div,k}$	Drift velocity for phase k [m/s]
$\vec{\nu}_m$	Mass-averaged velocity [m/s]
ρ_k	Density of phase k [kg/m^3]
ρ_l	Density of liquid phase [kg/m^3]
ρ_s	Density of solid phase [kg/m^3]
ρ_m	Mixture density [kg/m^3]
ρ_{water}	Density of water [kg/m^3]
σ	Surface free energy [J/m^2]
$\bar{\bar{\tau}}_{eff}$	Effective viscous stress tensor [N/m^2]
$\varnothing$	Heterogeneous degree [–]
φ	Contact angle [rad]

Abbreviations

CFD	Computational fluid dynamics
CMC	Carboxy-methyl cellulose
CNT	Classical nucleation theory
HS	Horizontal scheme
HTF	Heat transfer fluid
HXCR	Heat exchange capacity rate
PCM	Phase change materials
PISO	Pressure-implicit with splitting of operators
PRESTO!	Pressure staggering option
TES	Thermal energy storage
SA	Sodium acetate
SAT	Sodium acetate trihydrate
SM	Solidification and melting
VOF	Volume of fluid
VS	Vertical scheme

1.1. Heat storage unit

There are three major heat storage types: sensible, latent, and sorption/thermochemical [6]. Heat can be stored in chemical substances without energy loss based on reversible reactions in thermochemical heat storage [9]. Latent heat storage materials, also called phase change materials (PCM), absorb heat as latent heat of fusion during the melting process. The solid-liquid phase change of PCM is the most widely used because of a smaller volume change and a higher latent heat compared to the liquid-gas and solid-solid phase change, respectively [10]. Moreover, the thermal energy storage (TES) system can be divided into diurnal TES systems and seasonal/long-duration TES systems according to the storage period. Short-term heat storage systems are charged during the day and discharged during the night. Long-term heat storage systems store excess heat in summer for later use during winter in low-temperature domestic applications [11]. Delalić [12] proposed a small-scale solar heating system with combined sensible and latent heat storage, in which the PCM in the tank keeps at nearly the same temperature level and provides heat to the consumer during the period with reduced energy supply (i.e., night, cloudy, or fog weather). Englmair [13] investigated a combined short and long term heat storage with sodium acetate trihydrate (SAT) in cylindrical tanks. The discharge power is limited during the PCM solidification process; therefore, parallel operation of modular heat storage units was recommended. Besides, the heat quality is low; thus, it is unsuitable for applications with operating temperatures higher than 80 °C. Preliminary results showed that the supercooled SAT could be used as a sensible heat storage with a capacity of 15.5 kWh, which is about 25 % lower than a water storage of the same volume. However, the latent heat of SAT can be stored for longer.

1.2. Sodium acetate trihydrate

Phase change materials (PCM) can be classified into organic (paraffin and non-paraffin), inorganic (salt hydrate and metallic), and eutectic (organic-organic, inorganic-inorganic, and inorganic-organic). Salt hydrate PCM with melting points of 7–120 °C are commercially available [14]. Xie reviewed and classified salt hydrates' applications in buildings:

hot water tanks, wallboards, refrigeration systems, and air conditioning systems [15]. Zhao and Wang [16] reviewed a salt hydrate short-term storage for space heating. Sodium acetate trihydrate (SAT) with a melting point of 58 °C, employed as short term thermal energy storage, could be suitable for distributed fan-coil heating, distributed underground heating, distributed radiator, and centralized fan-coil heating from the perspective of temperature requirements.

In contrast to organic materials with congruent melting and self-nucleation, salt hydrate melts incongruently at the melting point because of incongruent dehydration. Moreover, liquidus salt hydrates supercool due to poor nucleating properties [17].

Some salt hydrates show a large supercooling degree during the solidification process; for example, $Na_2SO_4{\cdot}10H_2O$ (melting point: 32.4 °C) supercools to 15–18 °C, $Na_2HPO_4{\cdot}12H_2O$ (melting point: 34–37 °C) supercools to 15 °C, $NaAc{\cdot}3H_2O$ (melting point: 58.2 °C) supercools to 20 °C [18], and $MgCl_2{\cdot}6H_2O$ (melting point: 80 °C) supercools to 30 °C [19]. There are many approaches to trigger the solidification of supercooled salt hydrates: nucleating agents [14,20], mechanical rollers [21], metallic surface [18,22], ultrasonic sound [19,23], seed crystal [24,25], and local cooling [26,27]. Additionally, the stable supercooling of salt hydrate facilitates seasonal and long-term heat storage [28]. Ma [29] studied a model of the solidification process of supercooled sodium acetate (SA) aqueous solution in a single tube container. The results showed that, by crystallization of the supercooled SAT, the heat transfer fluid (HTF) outlet temperature could reach 30.4–37.5 °C which is high enough for space heating.

The effective latent heat of the heat storage decreases when the phase separation occurs in the salt hydrate [30]. Adding extra water, thickening agents, and polymer additives are three approaches to solve the phase separation problem of salt hydrate. Kong [31] investigated the heat content of SAT with different types and amounts of additives. The heat contents of SAT, SAT with 42 % extra water, and SAT with 0.1–2 % (wt%) carboxy-methyl cellulose (CMC) are 162, 194, and 200–216 kJ/kg, respectively, after a period of supercooling. The measured heat content is significantly lower than the theoretical value of 230 kJ/kg at 20 °C, mainly due to phase separation. Dannemand [32] tested flat prototype heat storage units utilizing stable supercooling of SAT mixtures. The heat released from the supercooled SAT and water mixture drops from 194 kJ/kg to 179 kJ/kg after twenty test cycles, and the energy discharged from the mixture of SAT and CMC was stable at 205 KJ/kg after six test cycles. In another cylindrical latent heat storage unit with SAT composites, the heat exchange capacity rate during charge was significantly lower for the unit filled with SAT and additive (Xanthan rubber) compared to the unit filled with SAT and extra water. This was due to less convection in the thickened PCM after melting [33].

Wang [24] reported the thermal power and heat exchange capacity rate of a cylindrical SAT heat storage unit, and the ratio of successful stable supercooling in the designed storage unit was 66 %. TRNSYS simulations of a solar combi system with SAT heat storage units [34] showed that a solar fraction of 80 % for a low-energy house could be achieved in Danish climatic conditions. Englmair [35] proposed a heat storage prototype consisting of four 200 kg SAT storage units and a 735 L water tank in single-family houses. About 80 % of the latent heat of fusion was transferred from PCM units to the water tank within 5 h after solidifying the supercooled SAT.

1.3. Multiphase model

The remaining challenges for successful applications of PCM heat storage are low heat exchange capacity rate and high production cost of the storage unit. Therefore, better and cheaper heat storage designs are considered essential. As a powerful design and optimization tool, computational fluid dynamics (CFD) has been used by authors to optimize the design of a phase change material heat storage tank [36]. In the investigation, the solidification and melting (SM) model in Fluent was used. Verma and Singh [37] developed a mathematical model in Matlab to investigate the embedded PCM in a parallel-flow solar air heater. The phase change process of the PCM was achieved by the SM model as well. Coding might give more flexibility when defining the model parameters than what the commercial software allows; however, many assumptions were made, and the model was simplified to 2 dimension to save computing power. Besides the various limitations of the SM model, it is often tricky to determine the appropriate parameters of the model, for instance, the mushy zone constant [38].

The multiphase model does not have these limitations that challenge the SM model, therefore, has been extensively used to simulate PCM heat storage. Kasibhatla [39] investigated the melting process of a PCM capsule under the influence of air. The immiscible fluids PCM and air were modelled using a continuum surface force model in the open source CFD software, OpenFOAM. The authors concluded that the prediction accuracy of the multiphase model is acceptable. Negi [40] developed a multiphase numerical model in MATLAB to study a PCM-integrated solar heater design with or without fins. The developed model was validated with published experimental results of a flat absorber plate collector design with PCM. The Eulerian granular multiphase model in Fluent was used to evaluate the performance of a bed-flow heat storage system. The pressure and interphase exchange coefficients controlled the energy exchange between encapsulated paraffin and the air [41]. Moreover, volume of fluid (VOF) multiphase model can also be applied in free-surface or stratified flow. Shojaeefard [42] optimized the lateral fins structure of a PCM-based battery thermal management system by employing VOF multiphase model. The liquid fraction of the PCM was a function of the interpolation of solidus temperature and liquidus temperature. Bechiri and Mansouri [43] study the heat and fluid flow of the PCM melting process inside a vertical cylindrical tube. A constant temperature was applied to the cylindrical shell's external surface, the air-PCM interactions was treated using the VOF model. The enthalpy porosity formulation was employed to solve the energy equation in liquid and solid PCM regions. Hosseinizadeh [44] used the VOF multiphase model and the SM model to study interfaces between air and PCM and the phase change process of the PCM, respectively. The results showed that heat conduction was the dominant mode of heat transfer at the initial melting, while free convection enhanced the melting at the later stage. None of the aforementioned CFD investigations focuses on supercooling of the PCM. Supercooling of PCM makes it difficult to discharge the stored latent heat, therefore, is often considered a big disadvantage. However, by utilizing stable supercool of sodium acetate trihydrate (SAT), a combined short term and long term heat storage could be realized [13,26–28,31–36].

The aforementioned multiphase models can hardly model the long-term heat storage utilizing stable supercooling of salt hydrates. In Zhou and Han's work [45], the transformation between salt hydrate's two phases was successfully simulated by applying the classic nuclei theory in the Mixture multiphase model. The supercooled salt hydrate crystallization was triggered manually by loading a user-defined function (UDF) file in the Fluent. However, the crystallization cannot be triggered at a desirable time point in the program. Moreover, their sandwich type heat storage model is simplified to a square box, and the heat exchange of the heat storage was not directly modelled. Therefore, it was not possible to investigate the influence of the heat exchanger design on thermal performance of the heat storage.

1.4. Scope

In this research, a multiphase model of a shell and tube heat storage tank utilizing stable supercooling of SAT is developed. The model consists of a cylindrical tank filled with water as the heat transfer fluid and a number of PCM tubes placed inside the tank. The heat storage tank is especially designed with an aim to reduce storage costs, since it can be mass-produced. The phase change of SAT in the tubes and the heat transfer of water in the tank from and to the SAT in the tubes are calculated. A modified user defined function is implemented in the

model to trigger crystallization of supercooled SAT at a desirable time. The developed multiphase model is validated against measurements. The validated multiphase CFD model is used to calculate the thermal and fluid properties of the SAT heat storage tank during charge and discharge. The investigations elucidate thermal behaviour of the SAT heat storage in four processes: melting, supercooling, triggered crystallization, and solidification without supercooling. The novelties of this study are:

- Multiphase flow model of a shell and tube heat storage tank enabling design optimization of the storage tank
- Simulation method for triggered crystallization of supercooled SAT developed and validated

The added values of the paper are:

- Capability and reliability of a new multiphase CFD model validated and documented
- The fluid pattern and thermal characteristics of the heat storage tank determined, including the heat exchange capacity rate, charged heat, discharged sensible heat, discharge latent heat
- The melting behaviour of 6 typical tubes elucidated
- The heat transfer mechanisms of the PCM heat storage tank characterized.

2. Experimental setup

The SAT heat storage unit was constructed using 166 kg stainless steel and filled with 137.8 kg SAT PCM material. The patented SAT-based composite with liquid polymer and extra water was developed by HM Heizkörper GmbH Heating Technology. The SAT was filled in 112 vertical tubes connected to the manifold at the top of the tubes. The heat storage unit was sealed by a flange on the top where both the extra expansion volume and the tube for dropping SAT crystals were located. The total height of the stainless steel storage unit is 1.7 m, and the external diameter is 0.4 m. Each tube has a height of 1.52 m and an inner diameter of 0.0276 m. As the heat transfer fluid (HTF), 75 L of water was filled in the heat storage unit. The HTF inlet was installed close to the bottom, and the water outlet was mounted on the upper opposite side.

Fig. 1(a) displays the tank's exterior without insulation, and Fig. 1(b) illustrates the system operating principle during charge and discharge.

Ten thermocouples (Tci1–Tci5 and Tco1–Tco5) with an uncertainty of 0.5 K were placed at different heights on the external surface of the tank. The radial distance between points Tci and Tco is 0.4 m, and the heights from the ground to points Tci1–Tci5 are 1.3 m, 1.1 m, 0.9 m, 0.7 m, and 0.5 m, respectively. A thermopile with an uncertainty of 0.1 K was used to measure temperature difference between the inlet and the outlet of the HTF. A Brunata HGQ-1-R3 flow meter with an uncertainty of 2 % was installed to measure the water volume flow rate during charge and discharge.

Fig. 1(b) shows the flow diagram of the heat transfer fluid. The circulation volume flow rate of the heat transfer fluid is 7 ± 0.14 L/min. After exiting the heat storage tank, water is firstly cooled down by the heat exchanger connected to the cooling system. Afterwards, the low temperature water enters the heating loop. The heating loop consists of a temperature regulated electric heating element, a pump and an inner loop. The power of the electric heater is controlled based on the difference between the set point temperature and the outlet temperature of the heater. In the inner loop there is a constant high flow rate. The aim of the inner loop is to enable a precise temperature regulation of the electric heater. Water with a desired temperature then enters the heat storage tank and release or extract heat from the heat storage depending on whether it is a charge or a discharge operation. In a charge operation, the inlet water temperature is 365 K (92 °C), while it is 303 K (30 °C) in a discharge operation. During charge of the heat storage tank, the heat exchanger for cooling is running at the minimum power, while during discharge, the heat exchange for cooling is running at the maximum power. This is done to save energy consumption of the electric heating element.

The simulated results in Section 5 are compared with the measured temperature and energy, and the derived measurement uncertainties of energy are given in Section 3.6.

3. Methodology

3.1. Simplification of geometry

The actual geometry of the shell and tube heat storage tank was simplified to a semi-cylinder with a diameter of 0.4060 m and a height of 1.5834 m in the CFD model, as shown in Fig. 2. Simplified geometry of the heat storage unit and the illustration of heat transfer fluid inlet/outlet. Firstly, the curved surface at the top and the bottom of the heat storage was flattened. Secondly, only half of the whole unit was calculated to save computing power; thus, the half unit model was built with

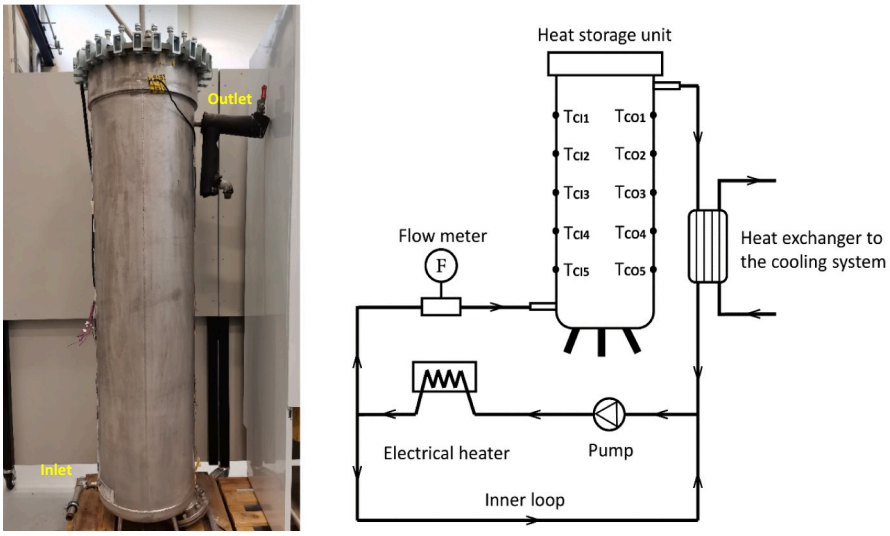

(a) Picture of the heat storage unit (b) Operating principle of charging and discharging processes

Figure 1. Experimental setup

Fig. 1. Experimental setup.

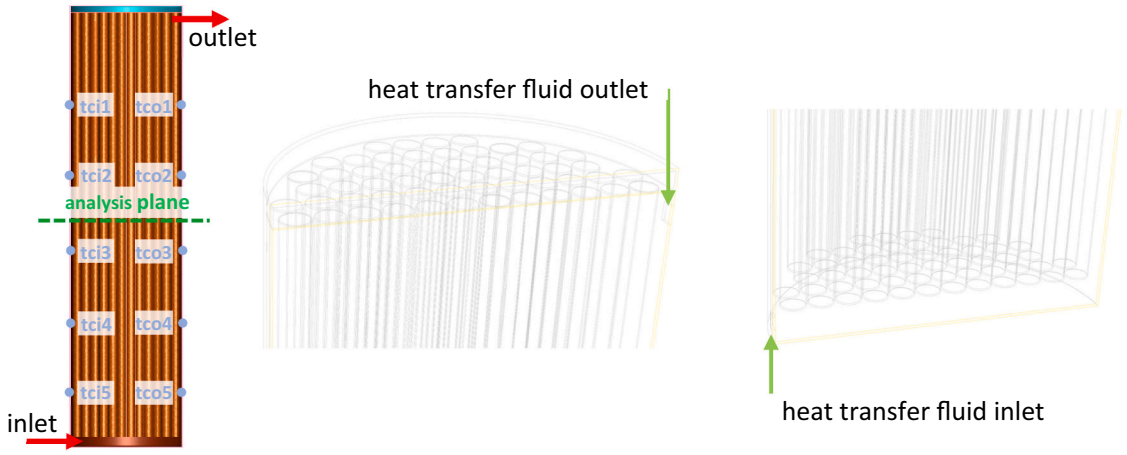

(a) *Symmetric plane* (b) *Details of the water outlet* (c) *Details of the water inlet*

Fig. 2. Simplified geometry of the heat storage unit and the illustration of heat transfer fluid inlet/outlet. (For interpretation of the references to colour in this figure, the reader is referred to the web version of this article.)

the symmetric surface cutting through the middle of the inlet pipe and the outlet pipe. Thirdly, the external diameter of 56 (half of the whole unit) inner tubes is 0.03 m, and the tube wall thickness is 0.0012 m. The effect of the storage insulation was considered in the convective heat transfer coefficient of the external tank walls. Finally, the positions of the ten thermocouples glued to the tank's external surface were evenly distributed on the height of the cylindrical heat storage unit, respectively, along the inlet side and the outlet side. In the simplified model, 69.6 kg SAT was filled in 56 inner tubes and the manifold, and 38 L water was used as the heat transfer fluid. The total mass of the stainless steel of the tubes and the tank wall was 83 kg.

3.2. Model meshing

Fig. 3 shows the mesh of the investigated model. Each tube has four mesh layers of inflation in the water zone and five mesh layers of inflation in the SAT zones. The mesh with 1.6 million cells and the maximum skewness of 0.64 was created. A grid independence investigation was carried out and shown in Section 4.1. Typical SAT tubes are chosen to illustrate melting and solidification behaviour of SAT. Fig. 4 illustrates the layout of the six selected SAT tubes from the top view. The position of the plane is shown as the analysis plane in Fig. 2. Tube #1 is located at the center of the heat storage unit; tubes #5 and #4 are the closest SAT tubes to the water inlet and the water outlet, respectively. Tubes #2 and #3 represent the peripheral tubes of the storage unit, and tube #6 stands for the other inner tubes.

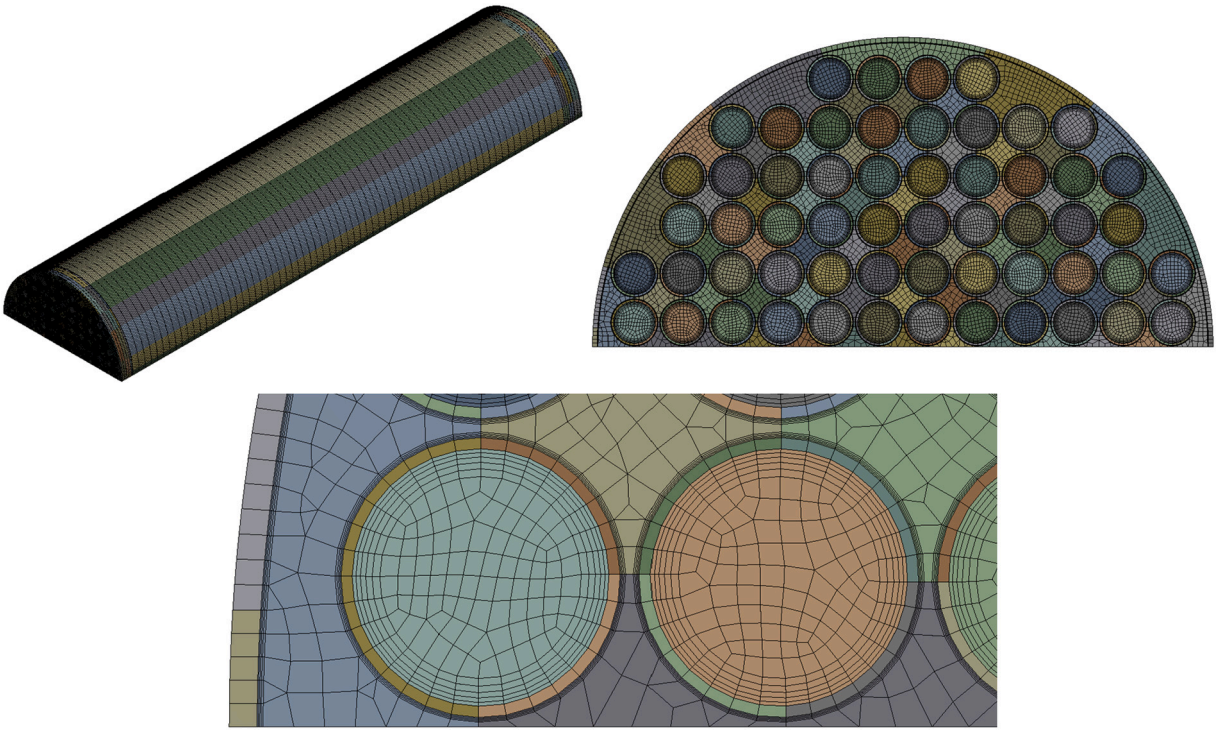

Fig. 3. Mesh pattern of the simplified geometry.

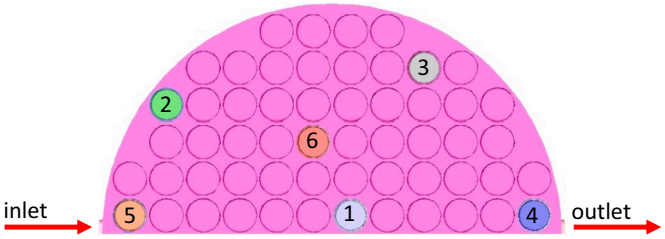

Fig. 4. Layout of 6 typical SAT tubes. Top view of the half manifold plate.

3.3. Boundary condition settings

The flow in the heat storage tank is largely laminar; therefore, a laminar model is used. The free stream temperature of the tank wall was set to the indoor air temperature (298 K), and a heat transfer coefficient of 3.3 W/m^{2} K was assigned to the tank wall. The inner surfaces of two adjacent zones were set as coupled thermal conditions. The water inlet was defined as a mass flow inlet with a mass flow rate of 0.058 kg/s; additionally, the time-series temperature of the inlet water was obtained from the experiment and used as input in the CFD model. The water outlet was defined as an outflow condition.

The properties of the materials applied in the multiphase model are listed in Table 1, and the Boussinesq model was used to calculate buoyancy driven forces for the solid and liquid SAT. Table 2 elaborates the parameters of the stainless steel used in the model, and the density was slightly adjusted to fit the total mass of stainless steel in the CFD model to the measured one.

3.4. Governing equations

In the Mixture multiphase CFD model, the SA aqueous solution (liquid phase), the SAT (solid phase), and water (heat transfer fluid) were set as the primary phase, the secondary, and the tertiary phase, respectively. Domain and thread structure hierarchy is special in the multiphase model. The super domain, the subdomain, and the interaction domain store properties and variables for the mixture of all phases, each phase, and the phase interaction mechanisms, respectively. When mixture properties and variables are needed (a sum over phases), the super domain is used for those quantities, while the subdomain carries the information for individual phases [46].

The governing equations are listed as follows [38]:

Continuous equation of mixture:

$$\frac{\partial}{\partial t}(\rho_m) + \nabla\cdot\left(\rho_m \vec{v}_m\right) = 0 \tag{1}$$

Table 1
Properties of 3 phases applied in the multiphase model.

Property	Expression		
	Liquid SAT	Solid SAT	Water
Density (kg/m^3)	$(\rho - 1340)g \approx -1340\beta(T - T0)g$	$(\rho - 1340)g \approx -1340\beta(T - T0)g$	$784 + 1.6595\,T - 0.0032\,T^2$
Reference temperature (K)	298.15	298.15	298.15
Specific heat Cp (J/kg K)	3020	2840	$5641–9.1467\,T + 0.0143\,T^2$
Thermal conductivity (W/m K)	0.34	0.55	$-0.3222 + 0.0046\,T - 5 * 10^{-6}\,T^2$
Viscosity (kg/ms)	$0.3673 - 0.001943\,T + 2.592 * 10^{-6}\,T^2$	$1 * 10^{8}$	$5 * 10^{11}\,T^{-5.954}$
Thermal expansion coefficient (1/K)	0.000512	0.000512	0.000512

Table 2
Properties of stainless steel applied in the multiphase model.

Property	Expression
Density (kg/m^3)	6566
Specific heat Cp (J/kg K)	500
Thermal conductivity (W/m K)	15

Momentum equation of mixture:

$$\frac{\partial}{\partial t}\left(\rho_m\cdot\vec{v}_m\right) + \nabla\cdot\left(\rho_m \vec{v}_m \vec{v}_m\right) = -\nabla p + \nabla\left[\mu_m\left(\nabla\vec{v}_m + \nabla\vec{v}_m^{T}\right)\right] + \rho_m\vec{g} + \vec{F} - \nabla\cdot\left(\sum_{k=1}^{n}\alpha_k\rho_k\vec{v}_{div,k}\vec{v}_{div,k}\right) \tag{2}$$

Energy equation of mixture:

$$\frac{\partial}{\partial t}\sum_{k=1}^{n}(\alpha_k\rho_k E_k) + \nabla\cdot\sum_{k=1}^{n}(\alpha_k\vec{v_k}(\rho_k E_k + p)) = \nabla\cdot\left(k_{eff}\nabla T - \sum_{k=1}^{n}\sum_{j}h_{j,k}\vec{J}_{j,k} + \bar{\bar{\tau}}_{eff}\cdot\vec{v}\right) + S_h \tag{3}$$

Liquid fraction equation for the secondary phases p:

$$\frac{\partial}{\partial t}(\alpha_p\rho_p) + \nabla\cdot\left(\alpha_p\rho_p\vec{v}_m\right) = -\nabla\cdot\left(\alpha_p\rho_p\vec{v}_{div,p}\right) + \sum_{k=1}^{n}\left(\dot{m}_{kp} - \dot{m}_{pk}\right) \tag{4}$$

PISO was employed as the pressure-velocity coupling scheme for the solution method, and the first-order upwind spatial discretization was implemented for the momentum, energy, and volume fraction equations. The gradient and pressure equations used least-squares cell-based and PRESTO! discretization methods in the calculation, respectively.

The first-order upwind scheme uses variables from the cell upstream as cell face values, while cell face values of the second-order upwind scheme are derived from two upstream cells. The former is acceptable when the flow is aligned with the mesh, although the second-order upwind is more accurate [38]. The first-order upwind scheme was applied in recent studies [47,48] from the perspective of efficiency and fair accuracy. The first-order upwind scheme is chosen in this study because it enables faster and robust convergence. Moreover, the heat storage model was divided into 1.6 million control volumes, which were dense and dominated by high quality hexahedral meshes. Furthermore, the fluid flow in the heat storage tank was mostly laminar. Using the first-order upwind scheme in multiphase flows saves computing power. In conclusion, although the first-order upwind scheme might not be the best discretization method, it is the optimal method for this study, balancing efficiency and accuracy of the calculations.

3.5. User-defined function for the phases change process

According to the classical nucleation theory (CNT), crystalline clusters form from the supercooled solution and then grow. The building blocks of crystals, namely crystalline nuclei, can attach to or detach from a cluster in a step-by-step manner to form macroscopic crystals [49].

Nucleation consists of homogeneous nucleation and heterogeneous nucleation.

As shown in Fig. 5(a), the rate of melting and solidification reaches equilibrium at point A, the melting temperature T_m. When the temperature is lower than T_m, solidus Gibbs free energy G_s is lower than the liquidus Gibbs free energy G_l. Therefore, driven by the Gibbs free energy difference $\Delta G_k = G_l - G_s$, the liquid phase crystallizes from point B to B′.

Assume the crystal nuclei as spheres with radius *r*, and the Gibbs free energy can be expressed as:

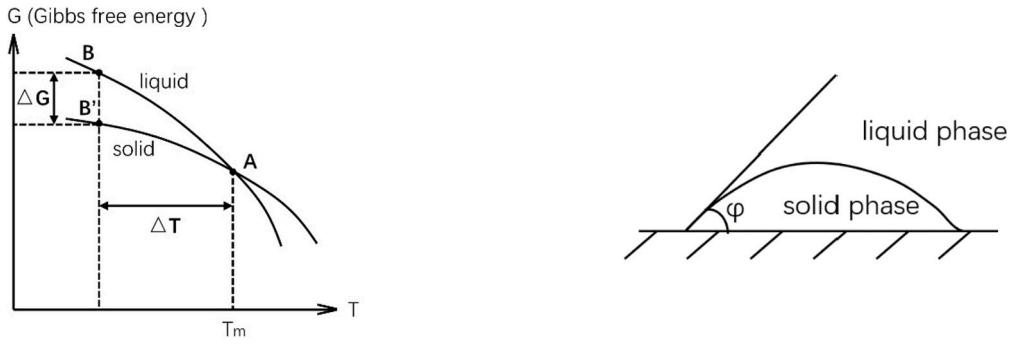

(a) Gibbs Free Energy of Solid Phase and Liquid Phase (b) Heterogeneous Nucleation

Fig. 5. Schematics of the phase change process.

$$\Delta G_k = \Delta G_v + \Delta G_s = -\frac{4}{3}\Pi r^3 \Delta G_{vv} + 4\Pi r^2 \sigma \tag{5}$$

Change of Gibbs free energy per unit volume is:

$$\Delta G_{vv} = \rho(\Delta H - T\Delta S) \tag{6}$$

Enthalpy change and entropy change during the solidification process:

$$\Delta H = H_s - H_l = H_m \tag{7}$$

$$\Delta S = S_s - S_l = \frac{H_m}{T_m} \tag{8}$$

Thus,

$$\Delta G_{vv} = \rho H_m \frac{\Delta T}{T_m} = \rho H_m \left|\frac{T - Tm}{Tm}\right| \tag{9}$$

The change of Gibbs free energy per unit volume increases with the degree of supercooling ΔT, which is the driving force of the phase change process.

According to the homogeneous nucleation theory, the Gibbs free energy change of heterogeneous nucleation [50] (illustrated in Fig. 5(b)) can be written as Eq. (10). In addition, the critical radius of the nuclei is negligible compared to the size of the wall. Thus, the control factor is a function of contact angle:

$$\Delta G_k' = \varnothing \Delta G_k \tag{10}$$

$$\varnothing = \frac{(2 + cos\varphi)(1 - cos\varphi)^2}{4} \tag{11}$$

It's easy to conclude that $\Delta G'_k$ is smaller than ΔG_k; consequently, heterogeneous nucleation has a smaller free energy barrier than homogeneous nucleation.

Thus, the mass transfer from liquid to solid phase $\dot{m}_{ls}$, the mass transfer from solid to liquid phase $\dot{m}_{sl}$, and the released/stored latent heat S_h are expressed as:

$$\begin{cases} \dot{m}_{ls} = 0 \\ \dot{m}_{sl} = 0, \quad 0 < t_b < t_0; \\ S_h = 0 \end{cases} \tag{12}$$

$$\begin{cases} \dot{m}_{ls} = \alpha_l \varnothing \rho_l \dfrac{\Delta T}{T_m} = \alpha_l \varnothing \rho_l \left|\dfrac{T - Tm}{Tm}\right| \\ \dot{m}_{sl} = -\alpha_l \varnothing \rho_l \dfrac{\Delta T}{T_m} = -\alpha_l \varnothing \rho_l \left|\dfrac{T - Tm}{Tm}\right| \\ S_h = H_m \dot{m}_{ls} \end{cases}, \quad T \le T_m \text{ and } \begin{cases} t_a > 0, or \\ t_b \ge t_0 \end{cases}; \tag{13}$$

$$\begin{cases} \dot{m}_{sl} = \alpha_s \varnothing \rho_s \dfrac{\Delta T}{T_m} = \alpha_s \varnothing \rho_s \left|\dfrac{T - Tm}{Tm}\right| \\ \dot{m}_{ls} = -\alpha_s \varnothing \rho_s \dfrac{\Delta T}{T_m} = -\alpha_s \varnothing \rho_s \left|\dfrac{T - Tm}{Tm}\right| \\ S_h = -H_m \dot{m}_{sl} \end{cases}, \quad T \ge T_m \text{ and } \begin{cases} t_a > 0, or \\ t_b \ge t_0 \end{cases} \tag{14}$$

where: t_a is the elapsed time during charge, t_b is the elapsed time during discharge, and t_0 is the time point when the crystallization is activated.

Eqs. (12)–(14) describe the mass and heat transfer during phase change of SAT. During cooling of SAT with supercooling, there is no crystallization of SAT even though the liquid SAT temperature is well below the melting point T_m, as shown in Eq. (12). After crystallization is activated (t_0), the transformation of liquid SAT into the solid phase is driven by the supercooling degree ($T - T_m$) during the solidification process. The released energy source S_h is then used to heat up the heat storage, as shown in Eq. (13). While during melting of SAT, the energy source S_h is determined by the amount of solid SAT transformed into the liquid phase, which is driven by the temperature difference (T − Tm) as well.

In the user-defined function file, the measured melting point of SAT (326 K, 53 °C) and the measured latent heat of fusion (198 kJ/kg) [24] were used.

3.6. Calculation

Charge power and discharge power of the heat storage in W are determined by:

$$P = c_{p,water} \bullet \rho_{water} \bullet \dot{V}_{water} \bullet (T_{in} - T_{out}) \tag{15}$$

Taking measurement uncertainties for specific heat of water (2 %), density of water (2 %), volume flow rate (2 %) and temperature difference (0.1 K), the relative uncertainty of the measured charge and discharge power is calculated to be 3.9 % under typical operation condition.

The heat exchange capacity rate (HXCR) of charge and discharge in W/K is estimated by:

$$HXCR = \frac{P}{T_{htf} - T_{sto}} \tag{16}$$

T_{htf} and T_{sto} are the heat transfer fluid's average temperatures and the PCM's average temperature, respectively.

The stored and released heat of the heat storage unit is obtained by integration of the following equation over the test period:

$$E = (P - P_{loss}) \bullet \Delta t = P \bullet \Delta t - h_{conv} \bullet \left(\frac{T_{in} + T_{out}}{2} - T_a\right) \bullet S \bullet \Delta t \quad (17)$$

P is the charge/discharge power of the heat storage in W. P_{loss} is the heat loss from the storage in W. Δt is the test period in second. The relative uncertainty of the measured energy derived from Eq. (17) is calculated to be 4.0 % under typical operation condition.

4. Investigation of mesh and time step independence

4.1. Investigation of mesh independence

Mesh independence was investigated by four meshes with 1.2 million, 1.6 million, 1.8 million, and 2.2 million cells, respectively. Inner layers in the SAT tubes of the scheme HS2 are denser than that of the scheme HS1. As a result, the vertical division of the model in the scheme VS2 is more than in the scheme VS1. The comparison of the mesh with 1.2 M cells (combined with HS1 and VS1) and 1.8 M cells (combined with HS1 and VS2) shows the influence of different vertical mesh densities on the simulation results. Adapting mesh in the horizontal and vertical directions gives the model with 1.6 M cells (combined with HS2 and VS1) and the model with 1.8 M cells (combined with HS1 and VS2). The mesh with 2.2 M cells combines the scheme HS2 and VS2.

4.1.1. Water outlet temperature

Fig. 6 shows simulated water outlet temperatures during discharge of the heat storage unit with different cell numbers. The right y-axis indicates the variations after vertical grid refinement from 1.2 M to 1.8 M cells (orange dash line) and from 1.6 M to 2.2 M cells (green line), and the variation between 1.6 M and 1.8 M cells (black dash-dot line).

The max variation of the different mesh schemes is −0.7 % (2.4 K) during the sensible heat releasing process. The water outlet temperature is slightly lower if the mesh grid is denser along the vertical direction. The variation is defined as $\frac{Ti' - Ti}{Ti}$. The water outlet temperature variations are less when the mesh cell numbers change from 1.2 to 1.8 million and 1.6 to 2.2 million. There is no significant influence of the mesh density on the calculated water outlet temperatures.

4.1.2. Z-velocity and temperature profiles at centerlines in SAT tube #6

Fig. 7(a) compares SAT's z-velocity in tube #6 on a horizontal centerline along the y-axis of the analysis plane (as shown in Fig. 2(a)) during discharge. As shown in Fig. 4, tube #6 in the center of the manifold is representative; therefore, it is used in the comparison.

The axial velocities of SAT in tube #6 are shown in blue squares and red circles for the mesh with 1.8 million cells and the mesh with 1.6 million cells, respectively. The SAT region, the tube wall, and the water region are indicated in the figure. It is shown that there is almost no significant difference in z-velocity profiles between the different mesh schemes. However, more inner boundary layers can precisely describe the near-wall SAT velocity gradient. At the early stage of the discharging phase (1200 s), as shown in Fig. 7(a), peripheral SA aqueous solution is cooled down by surrounding low-temperature water, while the inner part of the SA in the tube rises due to buoyancy force. This convection flow increases the heat transfer between water and SAT. The convection flow decreases gradually with a decrease in the SAT temperatures.

The simulated z-velocity (axial movement) and temperatures of SAT in tube #6 along the vertical centerline are shown in Fig. 7(b) and (c), respectively. The simulated results show the same trend along the z-axis. Consistent with Fig. 7(a), the inner part of SAT tube #6 lifts at the initial discharging phase (1200 s) and tends to be stationary at the end of the sensible heat discharging process (4200 s). Moreover, affected by the surrounding low-temperature water, the temperature of the lower part of SAT tube #6 drops at the 1200s, and the upper part of the tube cools down at the 4200 s.

4.2. Investigation of time step

Time-step size independence was also investigated by simulating three time-step sizes: 0.5 s, 1 s, and 2 s. Fig. 8 shows evolution of water outlet temperatures calculated with the different time steps during discharge of the heat storage. No significant difference is observed in Fig. 8 when applying different time-step sizes in simulations. The maximum influence of the time-step sizes on the water outlet temperature occurs during the sensible heat discharging process. After an increase of the time step to 1 s, there is almost no change of the predicted outlet temperature, except in 1750s–3000s where the outlet temperature increased by max. 0.7 %. The maximum variation of temperature prediction increases to 1.1 % with a time step of 2 s. There isn't any notable difference in outlet temperature prediction during initialization of crystallization if a time step of 1 s or 2 s is used instead of a time step of 0.5 s. Therefore, a time-step size of 1 s was chosen in the following simulations to save computing time.

5. Results and discussion

The fluid pattern and thermal characteristics of water and SAT in the heat storage tank are analysed. In addition, the heat transfer mechanism is elaborated, and the heat exchange capacity rate is determined.

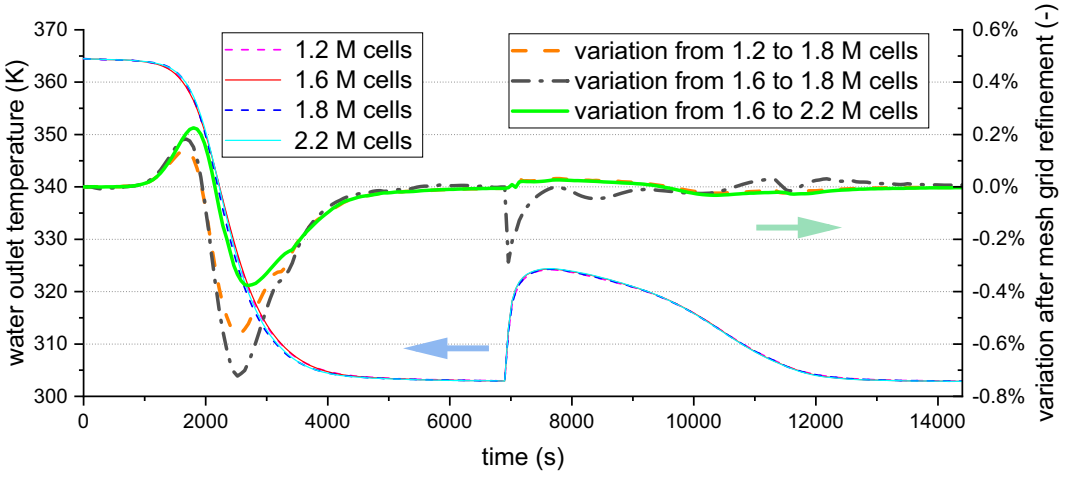

Fig. 6. Evolution of water outlet temperature during the discharging process using different grids. (For interpretation of the references to colour in this figure, the reader is referred to the web version of this article.)

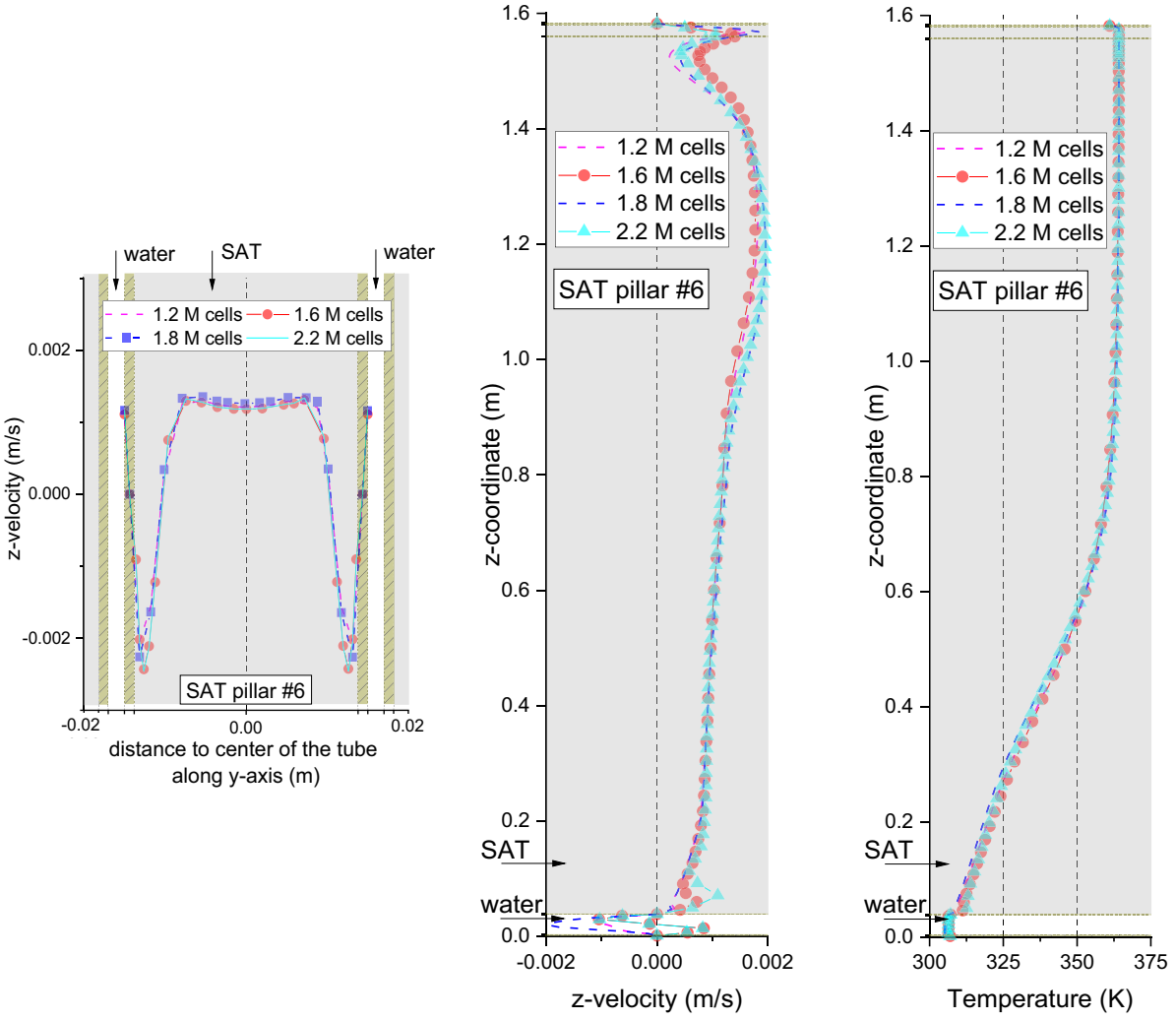

Fig. 7. Calculated Z-velocity and temperatures of SAT tube #6 in the early stage of discharge (at times 1200s). (For interpretation of the references to colour in this figure, the reader is referred to the web version of this article.)

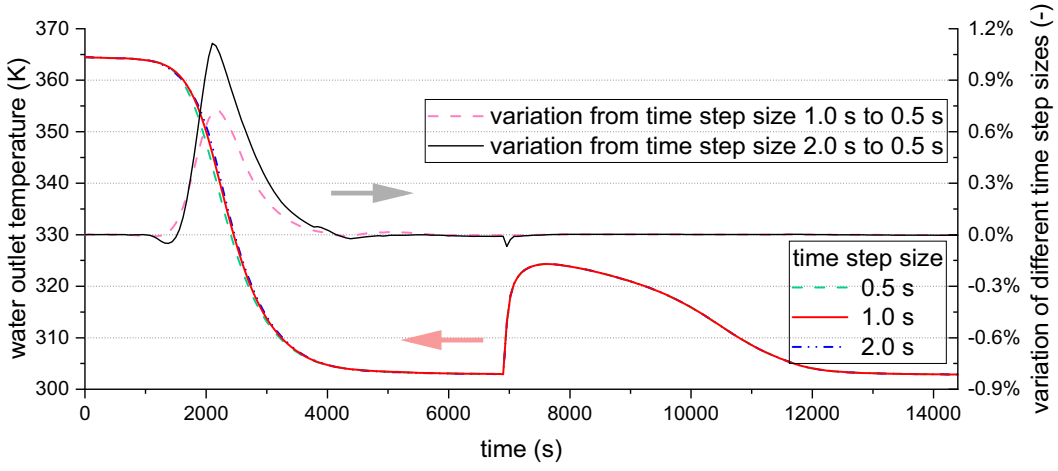

Fig. 8. Evolution of water outlet temperatures during the discharge with different time-step sizes.

5.1. Temperatures

5.1.1. Charge of the heat storage tank

The model accuracy is evaluated by comparing the CFD model with the experiments. The outlet temperature and the external surface temperatures of the tank are used in the comparison. The location of the ten surface temperatures is shown in Fig. 2(a) as blue dots tci1–tci5 and tco1–tco5.

Fig. 9 shows the development of the measured and simulated water outlet temperatures during the charging process. The simulation error is defined as the relative difference between the CFD calculated and the measured temperatures in Kelvin. The measured water inlet temperature was used as input in the CFD model. Except for the start of the charging phase, the simulation error of the water outlet temperature does not exceed ±1 % (2.9 K).

The ten thermocouples are evenly placed at different heights of the external surface of the tank and covered by insulation. The simulated temperatures at the ten sensor points are compared to the measured ones to gain insight into the model accuracy at different heights of the heat storage unit. For simplicity, the results of 6 selected points are shown in Fig. 10.

Fig. 10(a) shows 3 points with different heights on the inlet side: the highest (tci1), the middle (tci3), and the lowest (tci5). Similarly, Fig. 10 (b) shows the 3 points with different heights on the outlet-side external surface: the highest (tco1), the middle (tco3), and the lowest (tco5). The dash-dot line and the thick line represent the measured temperature and the simulated temperature, respectively. The period from 3000 s to 21,000 s after the start of the charging process is shown. The simulated temperature at the lowest point tci5 shows the maximum relative difference of −1.2 % at the initial part of the latent heat releasing process in Fig. 10(a). In Fig. 10(b), the highest point tco1 shows the maximum relative difference of −1.4 %, and the lowest point tco5 presents the maximum relative difference of 2.1 %.

It is shown that the CFD model predicts the temperatures on the inlet-side tank wall more actually than for the outlet-side tank wall. Moreover, on the outlet side, the CFD model underestimates the tank wall temperatures in the upper part of the tank, while it overestimates the temperatures in the lower part. This might be caused by the assumption of a laminar flow in the entire region, while the flow could be turbulent in limited areas of the heat storage.

5.1.2. Discharge of the heat storage tank

Fig. 11 compares the measured and the simulated water outlet temperatures and the relative differences during the discharging process. The discharge process consists of two phases: discharge of the sensible heat (0–6900 s) and discharge of the latent heat (6900 s–14200 s). In the first discharge phase, the outlet temperature of the heat storage decreases from 384 K to 304 K in 83 min. At the time 6900 s, solidification of the supercooled liquid SAT was triggered by an SAT crystal inserted from a vertical pipe mounted at the top of the tank. The heat of fusion of SAT is released. The maximum relative difference between the measurement and the simulation reaches 2.2 % (7.2 K) at 2340 s in the discharging process. The second peak value of the simulation error is 1.5 % (4.8 K) after triggering solidification of the supercooled SAT.

The measured external surface temperatures of the tank are compared to the calculated ones. The results of the three specific points on the inlet side are shown in Fig. 12(a), and those of the other 3 points on the opposite side are shown in Fig. 12(b). The black, blue, and red lines stand for the temperatures at the highest, the middle, and the lowest sensor positions, respectively. The period from 0 s to 12,000 s during the discharging process is shown.

During discharge of the sensible heat, the relative differences for the temperatures on the inlet-side external surface are within ±1.3 % (4.5 K) except the point tci5 at the start of the test. A larger simulation error exists on the outlet-side external surface. The simulation error reaches up to −3.8 % (13 K) at the highest position (tco1) near the water outlet.

During the latent heat discharge process, the maximum difference occurs after triggering the solidification. The simulated temperature is approximately 3.8 % (11.3 K) higher than the measured temperature at the middle points (tci3 and tco3) on both the inlet-side and outlet-side external surfaces. Afterwards, the simulated surface temperatures are lower than the measured ones, and the maximum difference reach −2 % at the peak value of the measured temperature at the middle height of the tank. At point tco1, the maximum error of the simulation reaches −2 % at the time 9600 s. By contrast, the maximum error of the point tci1 is −1 % at 8700 s.

Similar to the charge process, the CFD model predicts the temperature evolution on the inlet side more accurately than on the outlet side when there is a significant temperature change. The upper outlet-side surface temperature shows a relatively higher simulation error during the discharge of sensible heat. Moreover, during discharge of the latent heat, the model presents a more precise surface temperature at the lower part than the higher part of the tank. The peak value of surface temperature has the maximum error in the middle part of the tank, as indicated in Fig. 12.

In general, there is a good agreement between the CFD calculated and the measured temperatures, except for slightly higher differences at the start of the charge and discharge process.

5.2. The fluid pattern and thermal characteristics of water at the horizontal centerline

Fig. 13(a) displays the z-velocity (vertical movement) of water on the line shown as a green dash line in Fig. 2(a). The curves 1200 s, 7800 s,

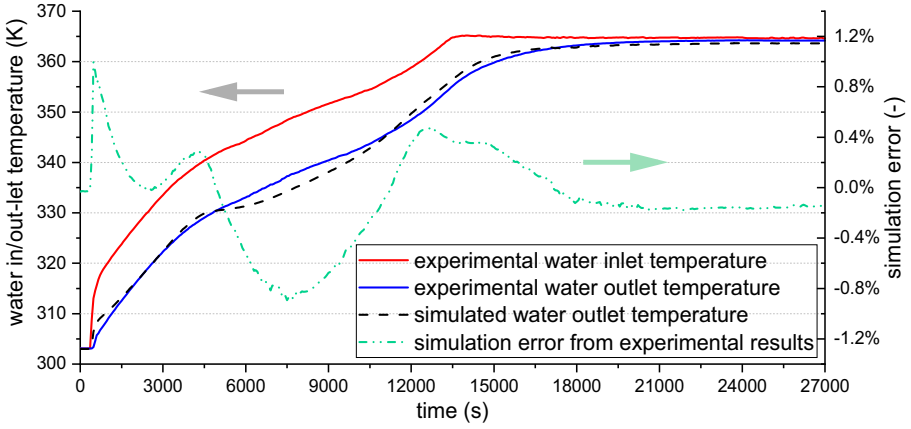

Fig. 9. Comparison of experimental and simulated water outlet temperature during the charging process.

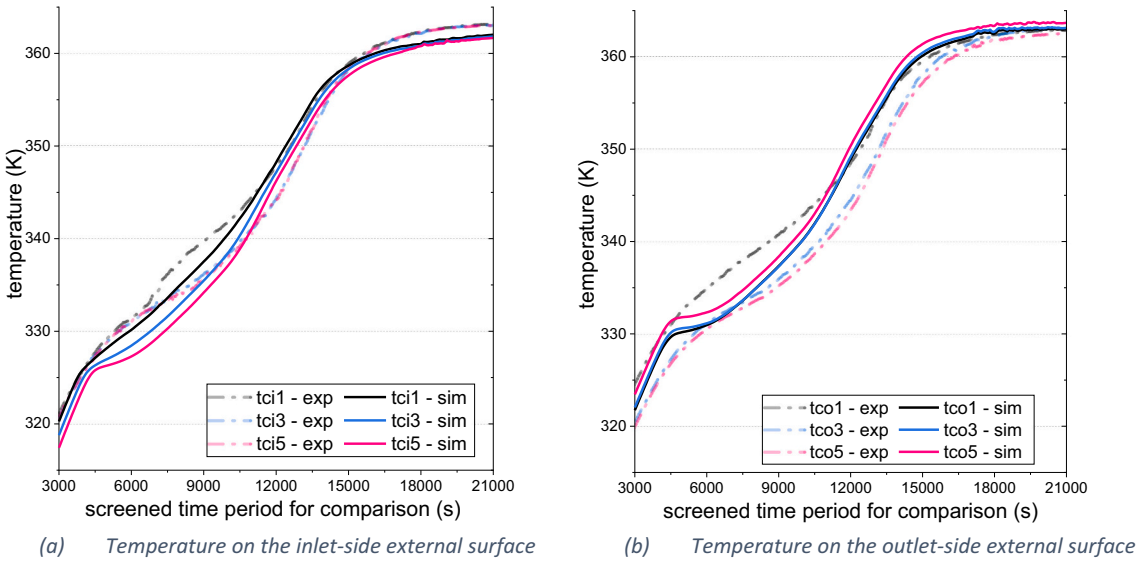

Fig. 10. Comparison of experimental and simulated surface temperature at typical sensor points during 3000 s–21000 s of the charging process.

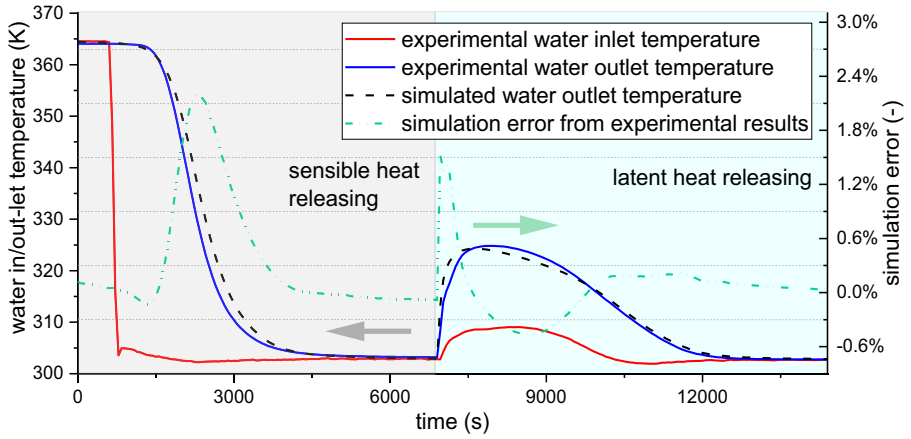

Fig. 11. Comparison of experimental and simulated water outlet temperature during the discharging process.

14400 s, and 27,000 s represent the initial stage of the sensible heat charge phase, the latent heat charge phase, the end of the latent heat charge phase, and the end of the charge phase, respectively. Fig. 13(b) shows the vertical movement at the start of the discharge of sensible heat (1200s), the sensible heat releasing phase (2400 s), the latent heat releasing phase (7800 s), and the end of the discharge (14,400 s). The location of the analysis line is shown in Fig. 13(b).

As shown in Fig. 13(a), there is an uneven flow distribution in the vertical direction on the analysis line. The presence of the tube walls causes the peak-valley-peak pattern of the vertical velocity. The negative z-velocity close to the inlet-side surface indicates a flow circulation in the tank. After entering the tank, the inlet hot water forms a jet flow. Because of the inertia, the inlet jet flows to the opposite before rising up. As a result, part of the water close to the inlet side was induced to flow downwards, forming a flow circulation. The same flow pattern can be seen more or less throughout the entire charge process. The circulation flow in the tank creates a shortcut for the inlet water before its heat is fully released. Therefore, it is considered a disadvantage for the heat storage.

The flow distribution in the tank is much better during the discharge process since cold water enters the bottom of the tank. At the end of the discharge process (14,400 s), a large fluid velocity is seen on the outlet side, but the influence on the thermal performance of the tank can be neglected.

Fig. 14 shows the temperature contours of the symmetric plane at different times. The hot HTF injected from the horizontally installed inlet rises due to the buoyant force, which leads to a well-mixed temperature distribution on the symmetry plane of the tank during the charge process in Fig. 14(a). While as observed in Fig. 14(b), there is a high degree of thermal stratification during the discharge because the cold water enters the bottom of the tank. The results show that unwanted flow circulation exists in the storage tank when there is a hot water inlet at the bottom.

5.3. The fluid pattern in SAT tubes # 1, 2, and 4 on the analysis plane

Figure 15, 16 and 17 show the z-velocity, the temperature, and the liquid fraction profiles in the SAT tubes on the analysis plane (indicated in Fig. 13(b)), respectively. SAT tubes #2, 3, 5, and 6 present similar flow and thermal behaviour on the analysis plane during the charge; therefore, tube #2 is representative. Tube #1 locates at the center of the heat storage unit, and tube #4 adjoins the water outlet. The investigations show that the behaviours of the SAT tubes are pretty uniform during discharge; thus, only the discharging results of SAT tube #1 are shown.

In Fig. 15, the x and y axis show the x coordinate and y coordinate

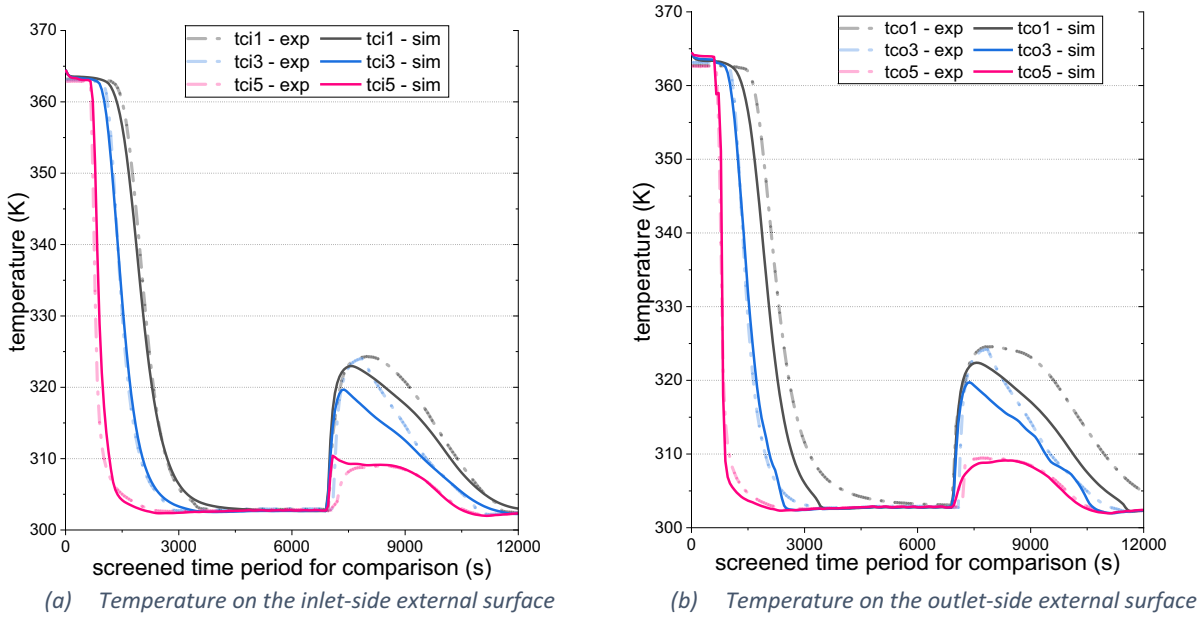

Fig. 12. Comparison of experimental and simulated surface temperature at typical points during 0 s–12000 s of the discharging process. (For interpretation of the references to colour in this figure, the reader is referred to the web version of this article.)

from the cell center, respectively. The result with the model of 1.6 million cells is shown. The colour represents the overall velocity in the cell. Moreover, as shown in the colour bar, the colour ranging from blue to red stands for a z-velocity from −0.01 m/s (downwards) to 0.01 m/s (upwards). The green colour indicates a vertical velocity close to zero. The black arrows attached to each point show the velocity vector of the liquid SAT on the analysis plane. Fig. 15(a) and (b) shows the velocity of each cell on the SAT analysis plane in the middle (9000 s) and the end (10,800 s) of the charge of the latent heat. In Fig. 15(c) and (d), the vertical and horizontal movement on the SAT analysis plane in the middle of the sensible heat releasing phase (1800s) and in the middle of the latent heat releasing phase (9000 s) are shown.

Similarly, the average temperature and liquid fraction are shown in Figs. 16 and 17. Different colours from blue to red stand for the temperatures ranging from 301 K to 346 K, and the liquid fraction from 0 to 1, respectively.

In the middle of the latent heat storing phase (9000 s), the maximum magnitude of the SAT horizontal velocity reaches 2.5×10^{-4}m/s, and the maximum z-velocity of SAT reaches 9×10^{-4}m/s in the SAT tube #4′, see Fig. 15(a). The vertical fluid velocity is larger than the horizontal velocity, meaning there is a natural convection flow in the tubes. The figure also shows different melting progress in the tubes due to different tube positions. During discharge of sensible heat (Fig. 15(c)), there is a much weaker vertical fluid velocity compared to that in the charging process. The inner temperature of SAT tubes remains at 326 K–331 K, and thus SAT in the inner part of the tubes stays solid at the transit phase, as shown in Fig. 17(a). The middle yellow circles in Fig. 16(a) stand for the melting temperature of 331 K, and the peripheral red points represent the heated SA aqueous solution. The melted peripheral SAT circularly flows along the inner wall of tube #4, which facilitates the heat transfer from the surrounding heat transfer fluid to SAT in the tube. However, it is also noticed that there is no significant full scale circulation inside the tube when SAT in the inner part of the tube is not completely melted, as shown in Fig. 15(a).

Fig. 15(b) shows that at the end of the charging process (10,800 s), the vertical fluid movement in the tubes is faster in tubes #1 and 4. The inner SAT is completely melted at the moment, as shown in Fig. 17(b). The buoyant force mainly drives the full scale flow circulation to a maximum speed of 0.01 m/s along the z-axis on the analysis plane. However, the horizontal fluid movement in tube #1 on the analysis plane has a different direction from that in tube #4. Different temperature distributions around the tubes could explain the difference.

Fig. 15(c), (d) illustrates the fluid pattern of the SAT tube #1 in the middle of the sensible heat releasing phase (1800s) and the middle of the latent heat releasing phase (9000 s). It is noticed that the discharging status of the 6 SAT tubes is simultaneous; therefore, tube #1 is representative. There is no noticeable arrow on temperature profiles on the analysis plane; however, the peripheral cooled SAT sinks at the rate of -2×10^{-3}m/s while the internal SAT floats up at the rate of 1×10^{-3}m/s because of the density difference. Therefore, the vertical flow along the inner tube wall accelerates the heat transfer from water to SAT by heat convection. At the time 9000 s, heat conduction dominated the heat transfer of the tubes because most of the tubes' SAT had solidified, as shown in Fig. 17(d).

5.4. *Thermal characteristics of six typical SAT tubes at horizontal and vertical centerlines*

Fig. 18 presents the volume averaged liquid fraction and the volume averaged temperature of the six typical SAT tubes during the charge and the discharge process. In Fig. 18(a), both temperature curves and liquid fraction curves of SAT tubes #2, 3, 5, and 6 overlap, while SAT tubes #1 and 4 melt in advance of the other tubes because the inlet water with relatively higher temperatures surrounds those tubes (#1, 4). As a result, the temperature of SAT tube #4 (dark green line) lifts firstly to the plateau, and the phase change process begins. The plateau temperature (326 K) is the melting temperature of the SAT mixture.

The curves of all six typical SAT tubes overlap in Fig. 18(b) during the discharge mainly because the water of similar temperatures surrounds all the tubes due to a high degree of thermal stratification in the tank. After solidification of the supercooled SAT is triggered, the average liquid fraction drops immediately to approximately 50 %.

Fig. 19 reveals the heat flow through the six typical tubes. The SAT tubes #2, 3, 5, and 6 overlap each other most of the time during the charging process, which means that the heat transfers through the wall of tubes #2, 3, 5, and 6 are simultaneous. At the time 4500 s, the heat transfer rate peaks at 80 W, which facilitates melting of SAT #4, which is shown as the lift of the green dash-dot line in Fig. 18(a) due to the

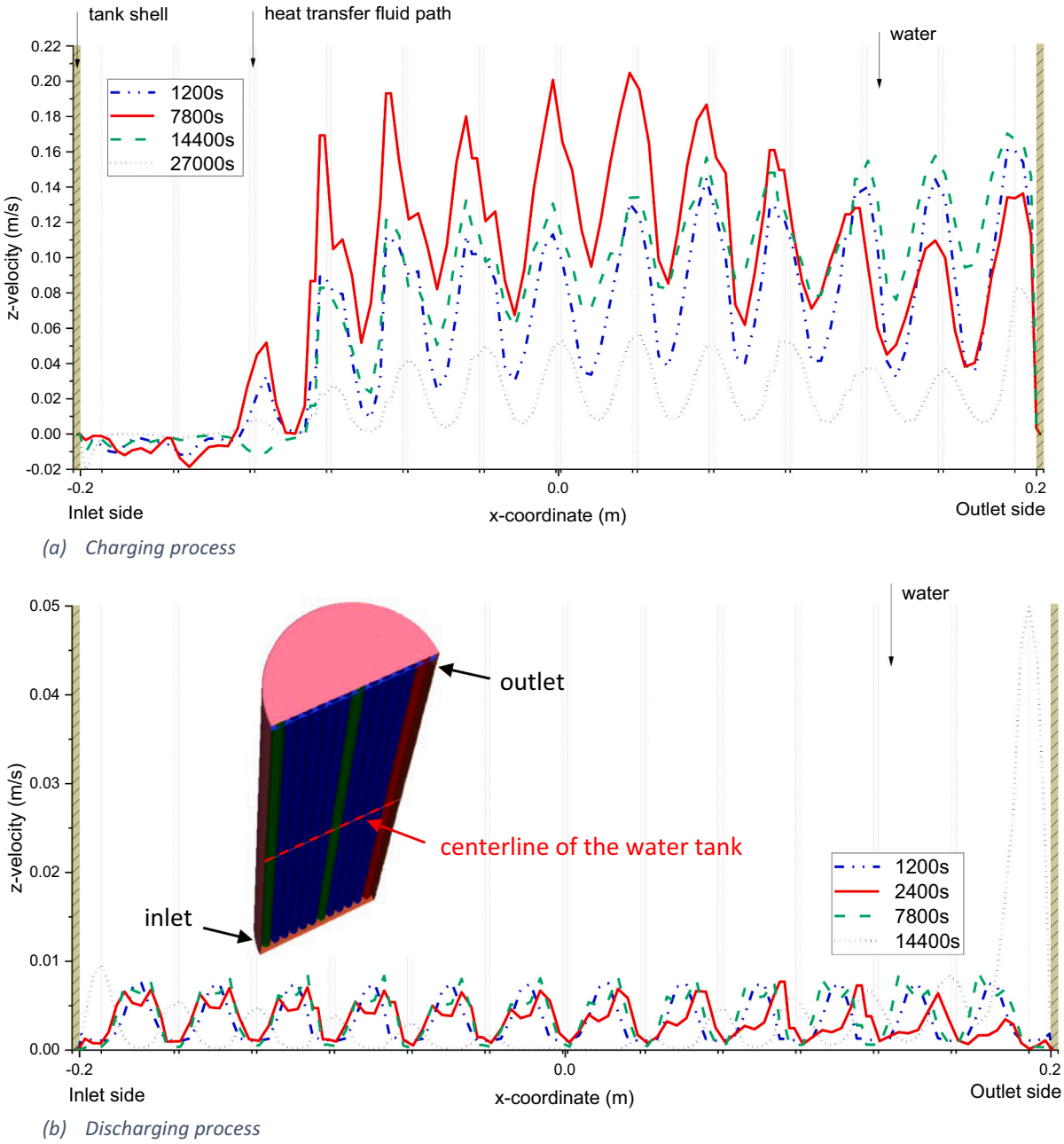

Fig. 13. Z-velocity profiles at the horizontal centerline of the water tank at different times.

surrounding hot water. Furthermore, the drop in the heat transfer rate of the SAT tubes #1 and 4 at around 9000 s indicates the end of the phase-changing process when the other four tubes are still melting. During discharge, the cold water enters the bottom of the tank and flows up to the top after being heated. The water region has a good thermal stratification (as shown in Fig. 14), meaning that the six SAT tubes experience similar temperatures. Consequently, the heat transfer rates of the six tubes are similar. Moreover, the model predicts a maximum heat flow of 380 W from the tube immediately after the start of the solidification.

Fig. 20(a) shows the liquid fraction at the vertical and horizontal centerlines of the SAT tubes. Tube #3 represents tubes #2, 5, and 6 due to the similar heating condition. At 7200 s (2 h) of the charge process, the bottom of the tube #1 melts firstly, and the bottom of tube #4 shows the tendency to melt. After half an hour, the liquid fraction of the lower part of the tube #4 reaches 100 %, while that of the upper part is approaching 80 %. This is due to the less well mixed water at the lower part of the tank and the relatively higher temperature fluid surrounding the tube #1. Meanwhile, the heated water floated up to the top, resulting in 100 % melting at the bottom and the top of the tube #1 and approximately 10 % of melting in the middle part of the tube. As for the other four tubes, only the upper part melts partly, as indicated by the blue dash line in Fig. 20(a). Fig. 20(b) shows the melting status of the tubes at the horizontal centerline with the z-coordinate of 0.8 m, where SAT melts from the peripheral to the center of tubes with the progress of the charging process.

Similarly, Fig. 21 plots the liquid fraction at vertical and horizontal centerlines during the discharge process. Unlike the charge, the tube position does not significantly influence the solidification status because of the horizontal even temperature distribution. The SAT solidifies from the bottom to the top of the tube after the solidification is triggered. The liquid fraction of vertical centerlines drops to 65 %. Furthermore, from Fig. 21(b), the solidification of SAT moves from the peripheral to the

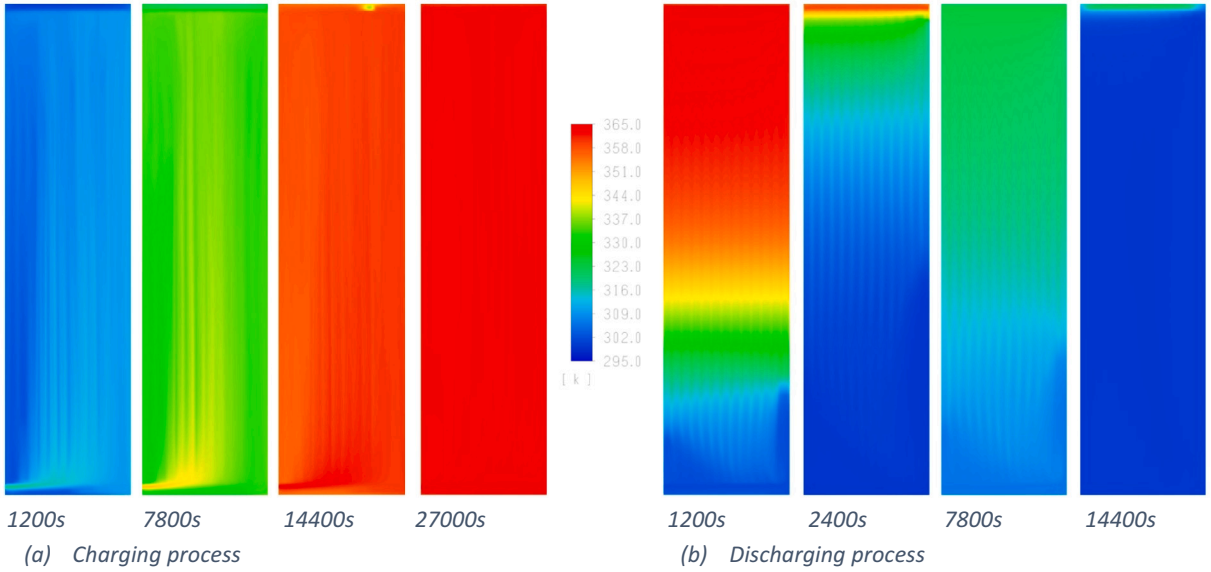

Fig. 14. Temperature contours of the inlet-outlet plane at different times.

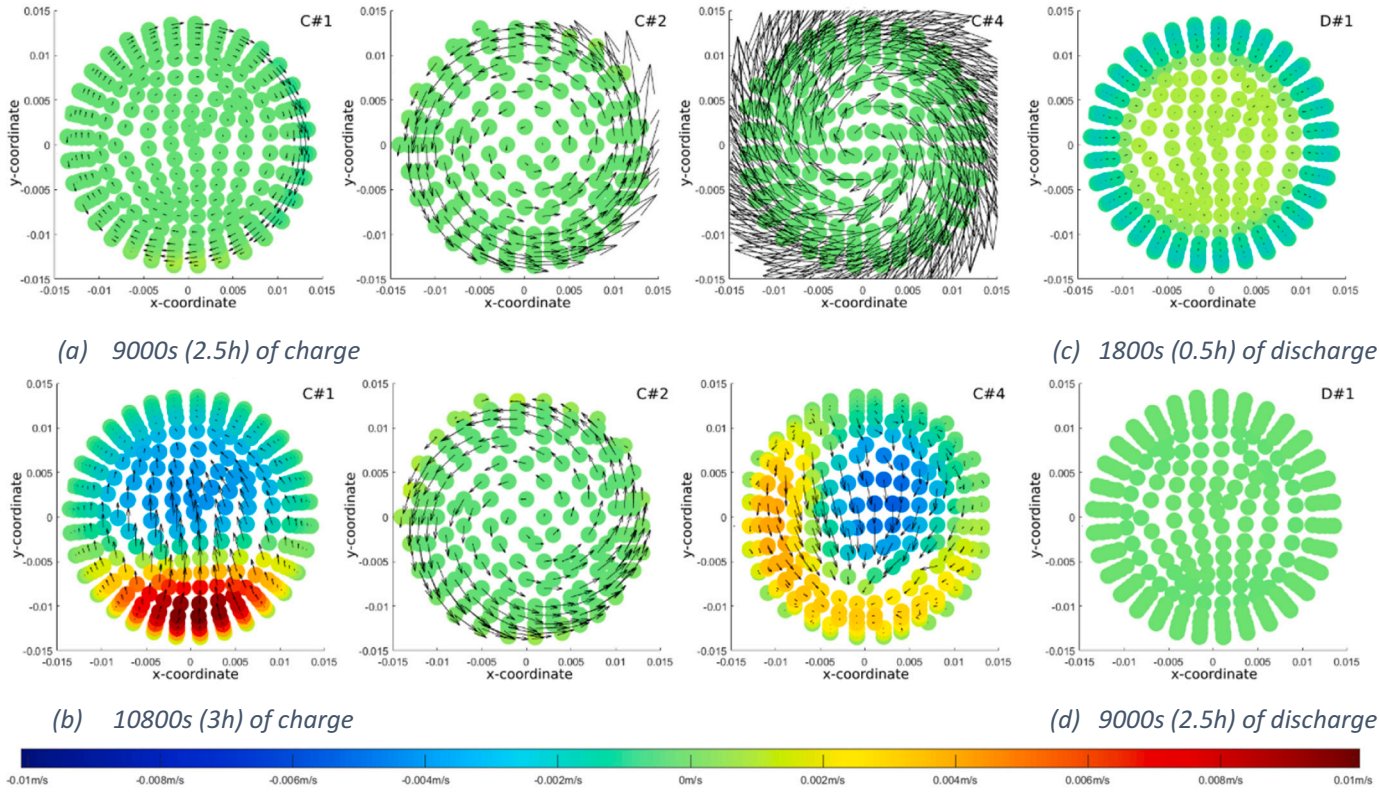

Fig. 15. Velocity profiles in typical SAT tubes on the analysis plane. (For interpretation of the references to colour in this figure, the reader is referred to the web version of this article.)

center of SAT tubes.

In conclusion, the position of the SAT tube influences its melting process. The tubes close to the inlet-outlet plane melt first because they are heated by hot inlet water in advance of other tubes due to buoyant force and the inertia of the inlet water. However, the SAT tubes adjacent to the inlet-side wall are the last to melt due to a lower temperature of the backflow of the circulation on the inlet-outlet plane. Therefore, the SAT tubes close to the water inlet have a similar melting process. This is because the unwanted circulation flow leads to uneven temperature distribution in the tank. By contrast, the discharge of the supercooled SAT is simultaneous in the tubes because of a higher degree of temperature stratification in the tank.

5.5. Thermal behaviour of the storage unit

The CFD predicted heat balance of the heat storage during the charge and discharge are shown in Fig. 22(a) and (b), respectively.

The heat loss (orange line) is negligible compared to the charging

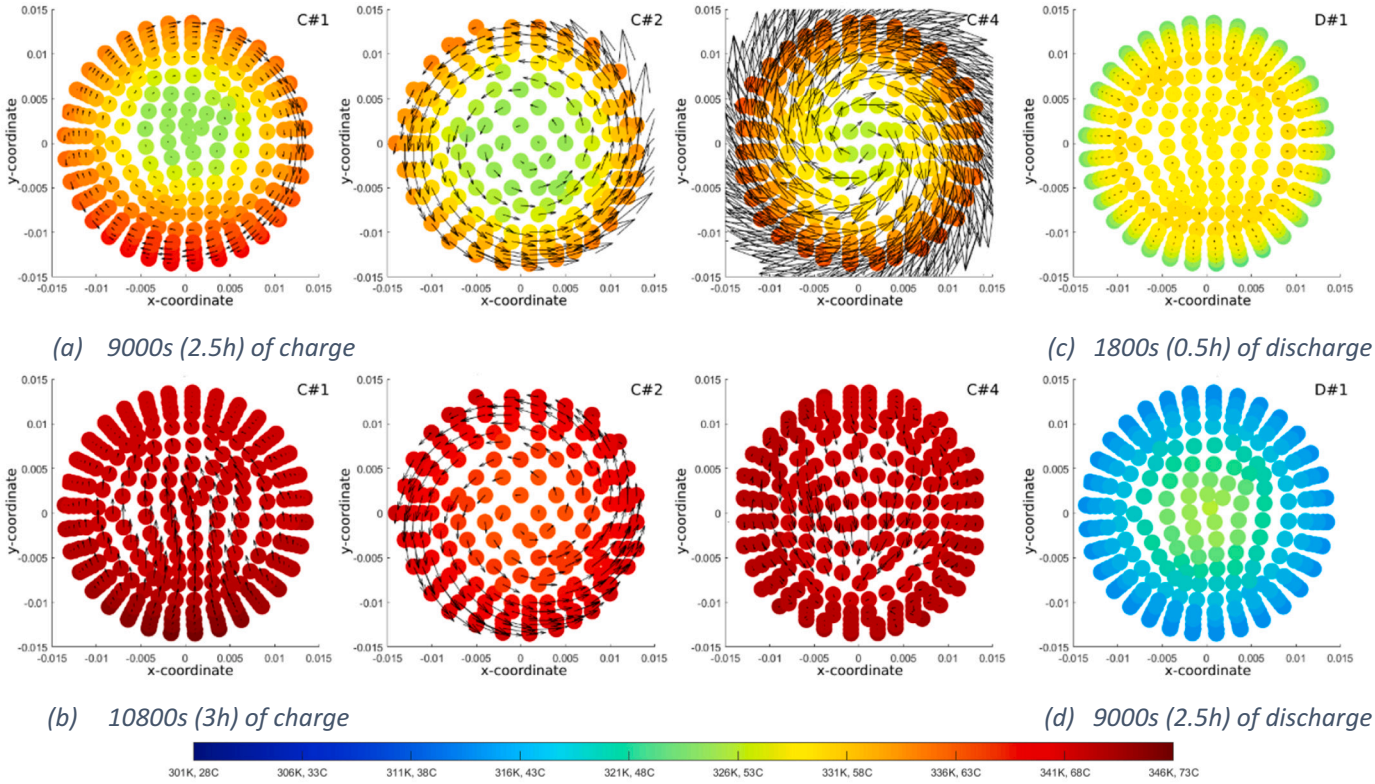

Fig. 16. Temperature and horizontal velocity profiles of typical SAT tubes on the analysis plane.

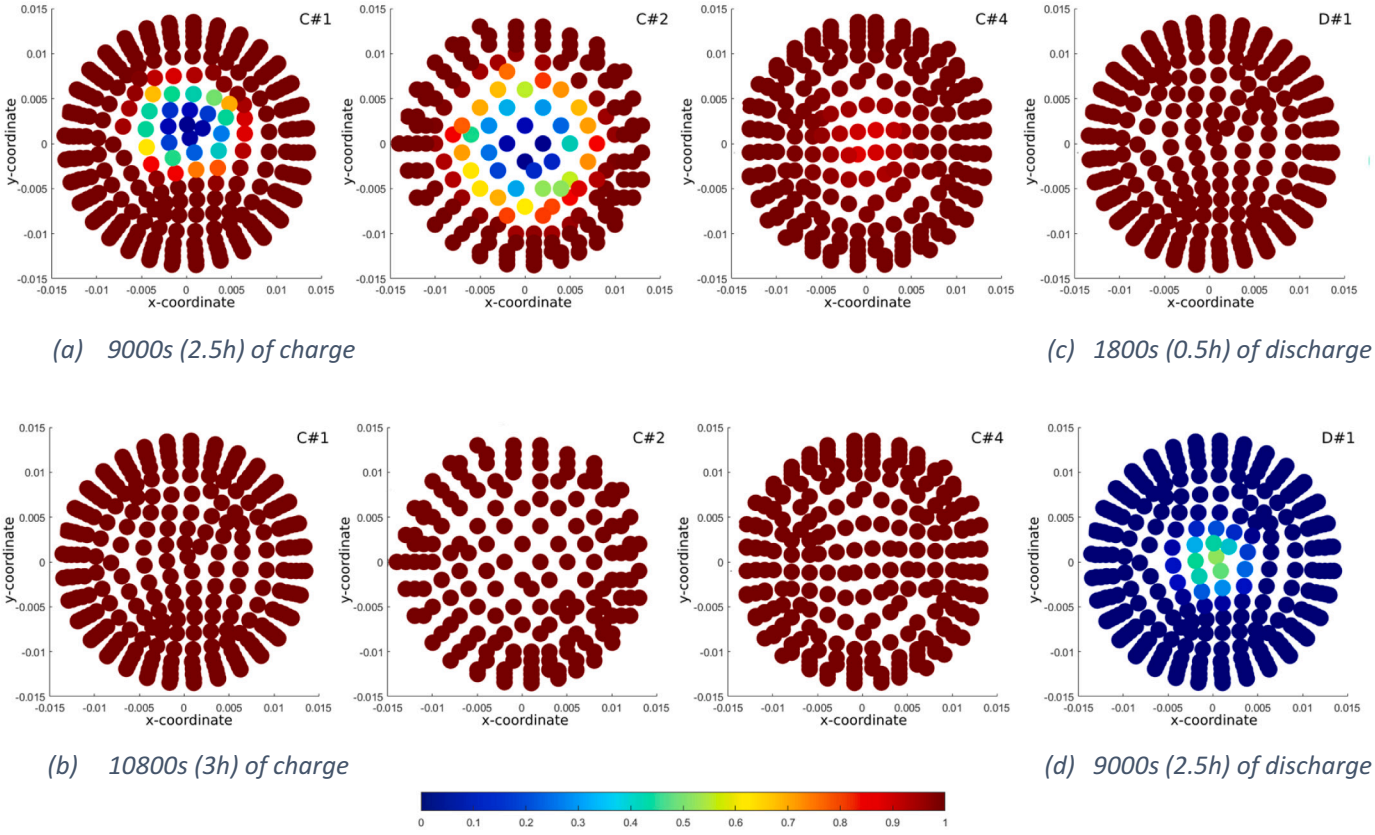

Fig. 17. Liquid fraction profiles of typical SAT tubes on the analysis plane.

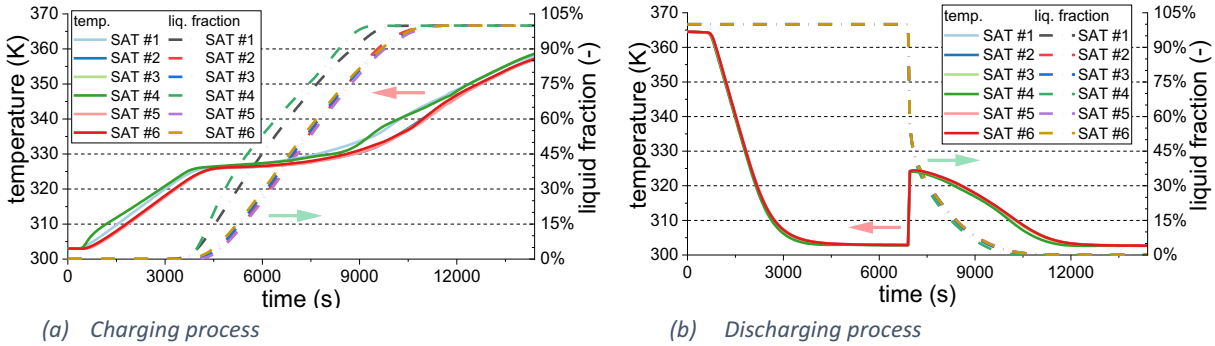

Fig. 18. Volume averaged liquid fraction and temperature evolutions of 6 typical SAT tubes. (For interpretation of the references to colour in this figure, the reader is referred to the web version of this article.)

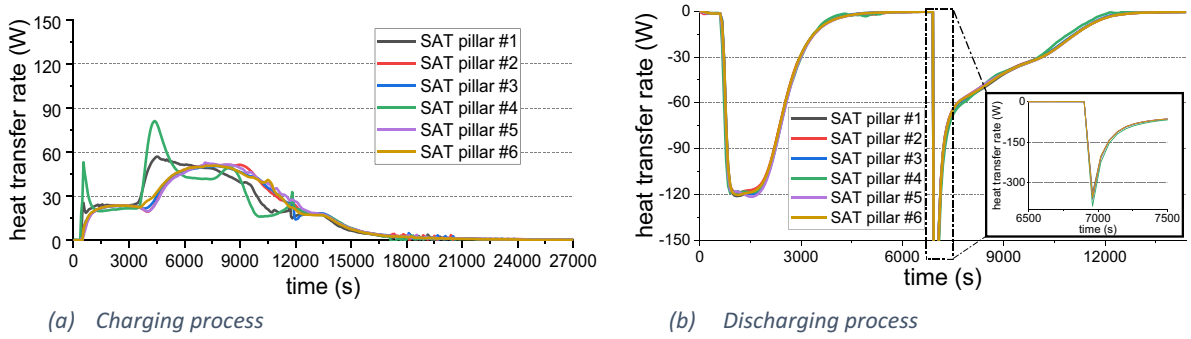

Fig. 19. Heat transfer rate evolution of 6 typical SAT tubes.

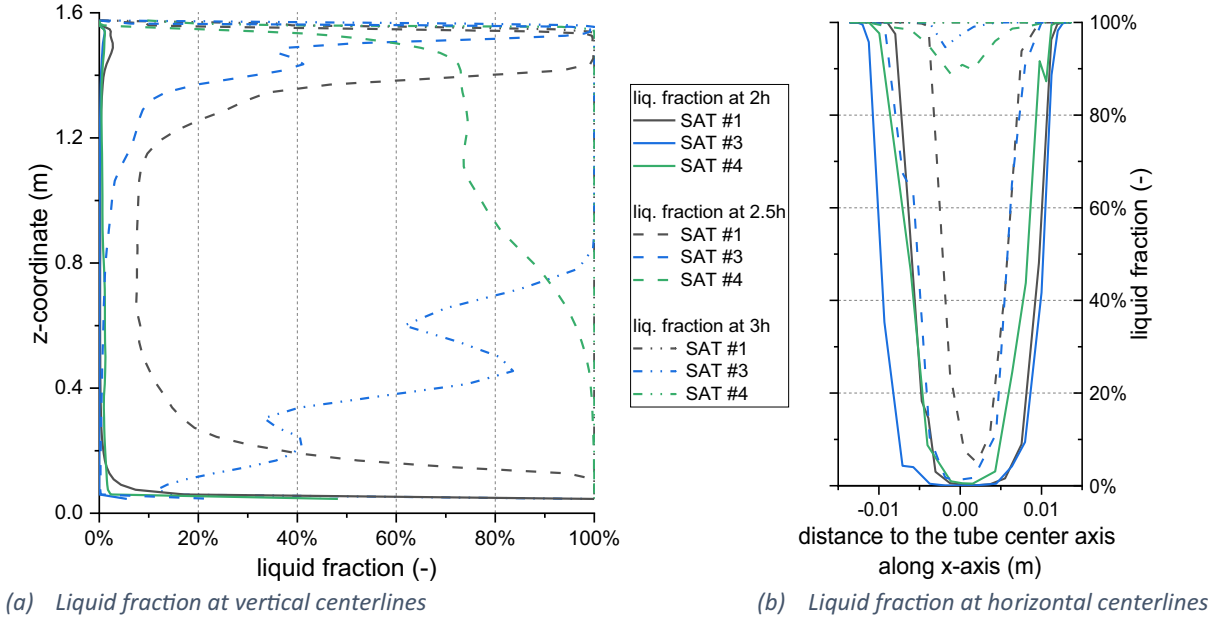

Fig. 20. Liquid fraction profiles in 6 typical SAT tubes at the time 7200 s, 9000 s, and 10,800 s of the charging process.(For interpretation of the references to colour in this figure, the reader is referred to the web version of this article.)

and discharging power. However, the heat loss also increases with an increase in the heat storage temperature. The first drop of the charging power at 4500 s occurs due to the decreased temperature difference between the inlet and outlet water caused by the unstable operation of the temperature control unit in the measurement. At that time, SAT begins to store the latent heat, and the volume averaged temperature enters a plateau in Fig. 18(a), which is indicated by the cyan-blue dash line in Fig. 22(a) from the perspective of the stored latent power. Hereafter, the temperature of the inlet water keeps increasing up to 364 K. It is worth mentioning that the latent heat storing phase is coupled with the sensible heat storing during the actual charging process, which can be explained by the incongruent melting of SAT.

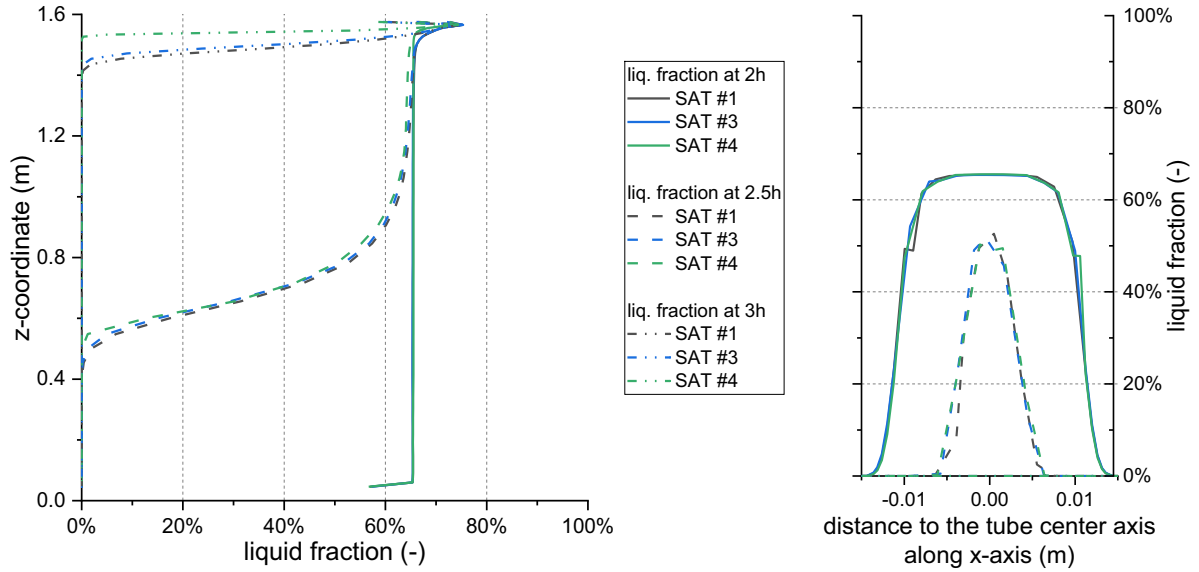

Fig. 21. Liquid fraction profiles in 6 typical SAT tubes at the time 7200 s, 9000 s, and 10,800 s of the discharging process.

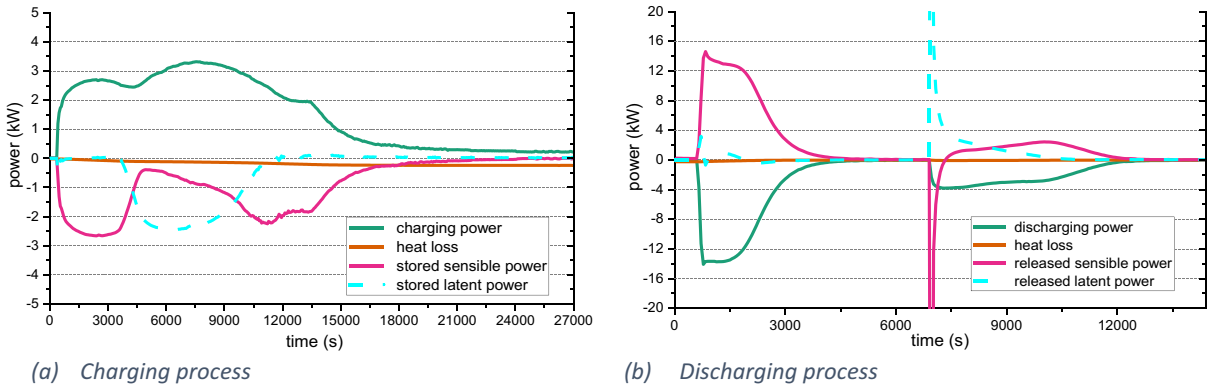

Fig. 22. Evolution of the dynamical heat balance of the half unit. (For interpretation of the references to colour in this figure, the reader is referred to the web version of this article.)

The peak discharging power is approximately five times that of the charging power in Fig. 22(b), caused by the thermal inertia of water and a larger vertical temperature gradient in the storage. The sensible heat is released before the solidification is triggered. While, during the solidification of the supercooled SAT, the released latent heat heats the heat storage unit. Afterward, the latent heat of SAT and sensible heat of the whole heat storage unit are discharged.

Fig. 23 shows the power and the CFD predicted heat exchange capacity rate (HXCR) of the heat storage unit during the charge and discharge, calculated by Eq. (16). The absolute values of the HXCR and power are presented in Fig. 23(b). Unfortunately, the HXCR is difficult to obtain from the measurement due to the difficulties of measuring

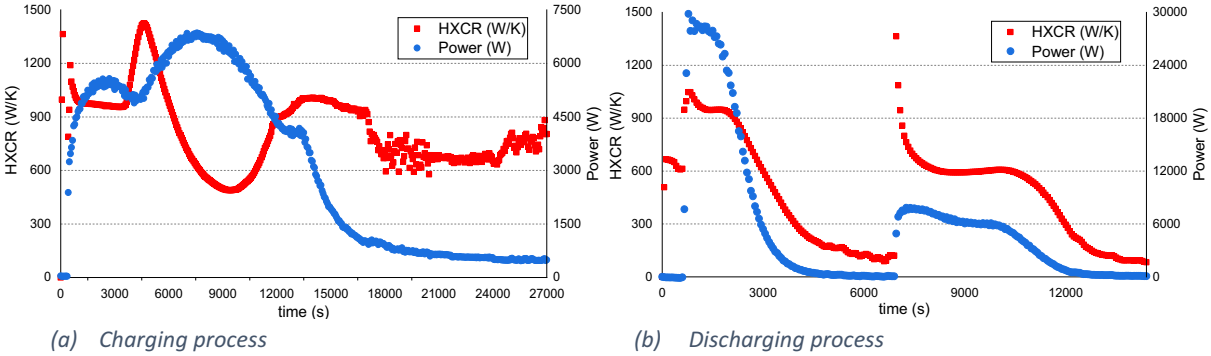

Fig. 23. CFD calculated heat exchange capacity rate of the heat storage unit.

average PCM and water temperatures.

As shown in Fig. 23(a), the CFD calculated HXCR reaches up to approx. 1364 W/K at the start of the charge due to the thermal inertia of water in the storage tank. The peak at 4500 s indicates melting of SAT close to the wall. With the progress of the melting boundary into the tube, heat has to transfer longer and longer distances, and the temperature difference between SAT and HTF increases notably, resulting in a significant drop of HXCR after 4500 s. After 9000 s, SAT has melted completely. Stronger natural convection in the tube increases HXCR. After 18,000 s, it approaches the end of the charging process. The temperatures of SAT in the tubes are well established, resulting in weaker natural convection flow and a slightly lower HXCR. The energy weighted average HXCR of the entire charge process is 850 W/K.

It is shown in Fig. 23(b) that the HXCR reduces from 1048 to 90 W/K during discharge of the sensible heat due to increased thermal resistance on the SAT side. After the triggering of the solidification, the HXCR raises to 1364 W/K. HXCR keeps at 600 W/K during the latent heat release. Afterward, there is a gradual decrease in HXCR because the heat transfer from the solid SAT to water becomes more and more difficult. The energy weighted average HXCR of the entire discharge process is 795 W/K.

In authors' previous investigations, the HXCR is calculated to be 390 W/K during charge and 750 W/K during discharge with a volume flow rate of 7 ± 0.14 L/min [36]. There is a slight difference in the HXCR during discharge but a large difference in HXCR during charge. The difference is caused by how the temperature difference between PCM and the heat transfer fluid is determined. In the current paper, the difference is determined by the average temperature of HTF minus the average temperature of SAT, while in [36], a log difference was used.

At the end of the charge, the CFD predicted charge energy is 21.15 kWh, with a difference of 0.01 kWh compared to the measured charge energy of 21.16 ± 0.85 kWh. The stored and released heat by measurement was calculated by Eq. (17). And the simulated discharge energy is 21.70 kWh with 14.05 kWh of sensible heat and 7.65 kWh of latent heat, compared to the measured discharge energy of 21.13 ± 0.85 kWh, the sensible heat of 13.57 ± 0.54 kWh, and the latent heat of 7.56 ± 0.30 kWh with differences of 0.57 kWh (2.7 %), 0.48 kWh (3.5 %), and 0.09 kWh (1.1 %), respectively.

Additionally, in this study the max. discharge power is 8 kW, which is significantly higher than those reported in the literature for other storage designs, for example, 5.0 kW [32], 4.8 kW [33], and 5.0 kW [51]. This is because the heat storage tank in the study was especially designed with a large heat transfer area of 16.2 m^2, while in the literature the heat transfer areas are 5.8 m^2 [32], 2.3 m^2 [33], and 3.4 m^2 [51], respectively.

Fig. 24 shows a breakdown of the CFD calculated energy contents of the heat storage. The energy percentage for each component is the ratio between the energy content of the component and the energy content of the entire storage. As shown in Fig. 24(a), at the start of the charging process, heat is used to heat up the water in the storage tank. Then the temperature of SAT increases gradually, increasing the sensible heat of SAT. Afterward, SAT starts to melt, and its share of the energy content increases significantly. After complete melting of SAT, the SAT temperature and water temperature rise, increasing sensible heat. At the end of the charge, approx. 69.3 % heat is stored in SAT (33.1 % sensible and 36.2 % latent), followed by water with a share of 24.2 %. The rest of the energy (6.5 %) is stored in the tank shell and the internal tube shells in the form of sensible heat. The energy breakdown of the storage unit at the end of the charge is listed in Table 3. The storage unit's energy breakdown at the start of the discharge is slightly different from that at the end of the charge due to different storage temperatures. Fig. 24(b) shows the energy content of each component during discharge. The sensible heats of SAT, water, and tube/tank material are discharged gradually. At the end of the discharge of sensible heat, only the latent heat of SAT is kept since SAT supercools. After triggering the solidification, 4.2 kWh of latent heat was transformed into sensible heat of SAT, water, tank shell, and tube shells within 7 min. Eventually, the latent heat was released completely.

5.6. Heat transfer mechanism between SAT tubes and heat transfer fluid

Fig. 25 illustrates the heat transfer mechanism during the charge and the discharge of the heat storage. The black upward arrows in Fig. 25(a) show water movements in between the tubes, whose velocity profiles are dominantly shaped by the resistance of the fluid path. In addition, Fig. 25(a) presents the latent heat charging phase. The SAT close to the tube wall melts first by heat conduction through the tube wall. As a result, the melted SAT close to the tube wall has a higher temperature, therefore flows upwards along the tube wall. In comparison, the liquid SAT close to the solid SAT with a lower temperature tends to flow downwards, forming a circulation in the region of the melted SAT. The noticeable vertical velocity superimposed on subtle horizontal speed results in a spiral flow path along the inner wall of the SAT tubes, which significantly increases the heat transfer rate between the HTF and the

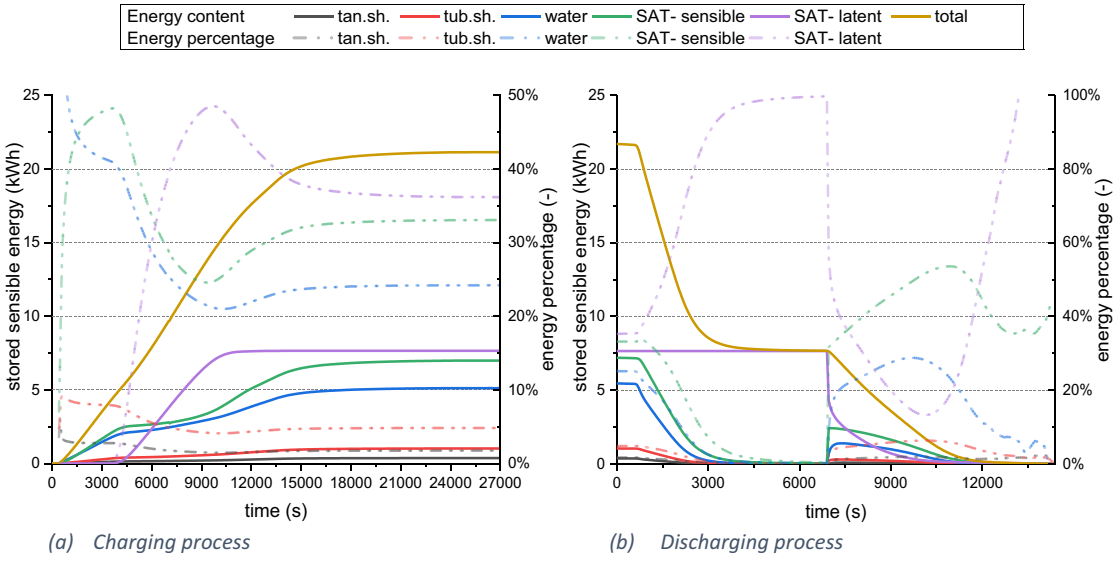

Fig. 24. Energy evolution of tank shell, tube shells, water, and SAT of the heat storage unit.

Table 3
Energy breakdown of the storage unit at the end of the charge and start of the discharge.

Items		Components					Total
		Tank shell	Tube shells	Water	SAT sensible	SAT latent	
Charge	Energy (kWh)	0.367	1.019	5.118	6.992	7.652	21.15
	Percentage (%)	1.7	4.8	24.2	33.1	36.2	100
Discharge	Energy (kWh)	0.375	1.043	5.450	7.180	7.652	21.70
	Percentage (%)	1.7	4.8	25.1	33.1	35.3	100

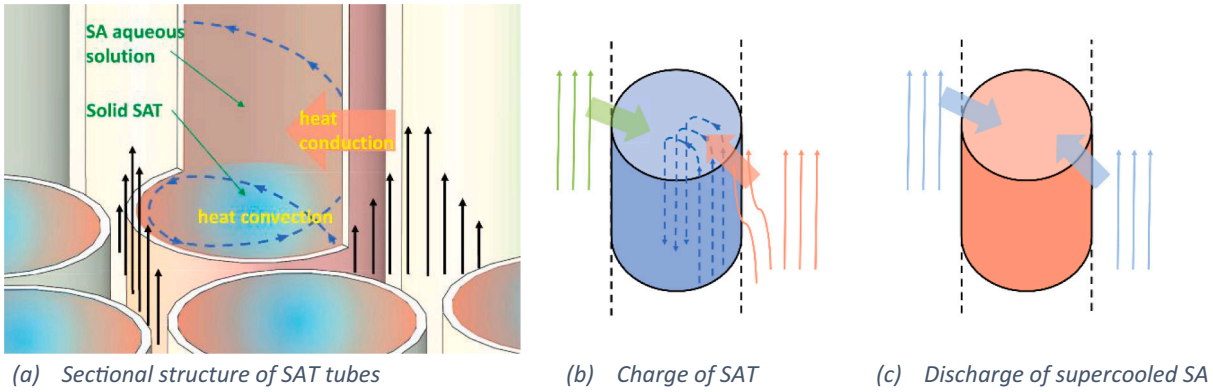

Fig. 25. Heat transfer mechanism within the heat storage unit.

SAT.

Fig. 25(b) and (c) shows a section of an SAT tube for simplicity. When the SAT in the tubes melts completely, the significant natural convection of liquid SAT in the vertical direction is driven by buoyancy force, as shown in Fig. 25(b). On the contrary, there is no noticeable fluid movement within the SAT tubes during the discharging process in Fig. 25(c) because there is a high degree of thermal stratification in the tank due to a cold-water inlet at the bottom of the tank. Therefore, heat conduction is the dominant form of heat transfer.

6. Conclusions

A shell and tube heat storage tank capable of both long and short term heat storage has been developed by utilizing stable supercooling of sodium acetate trihydrate. Theoretical and experimental investigations were carried out to determine the power, heat exchange capacity rate (HXCR), and the stored energy of the heat storage tank during the charge and the discharge. The following conclusions are drawn:

- The multiphase CFD model predicts temperatures of the heat storage satisfactorily.
- In the water region, there is a strong mixing during charge because the water inlet is located at the bottom of the tank. While during discharge, a higher degree of thermal stratification is seen.
- In some of the tubes, in the early phase of the charge, a spiral natural convection flow of the liquid SAT exists close to the tube wall, which significantly increases the heat transfer rate. Afterward, the circumferential flow diminishes, and a vertical natural convection flow dominates the tube. During discharge, all the tubes have similar thermal conditions because there is a high degree of thermal stratification in the tank.
- The charging power of the heat storage unit reaches a maximum of 6.6 kW with an inlet flow rate of 7 $\pm$ 0.14 L/min, while during discharge of the sensible heat, the discharging power reaches 27.2 kW, followed by 7.6 kW during discharge of the latent heat.
- The CFD predicted heat exchange capacity rate (HXCR) of the heat storage unit is 490–1100 W/K except for peak values of 1364 W/K due to the thermal inertia of the storage tank and 1424 W/K at the beginning of melting. When the heat storage is discharged, HXCR reduces from 1048 to 90 W/K during the sensible discharge and is approx. 600 W/K for discharge of the latent heat. The energy weighted average HXCR is 850 W/K and 795 W/K during charge and discharge of the heat storage, respectively.
- The CFD model shows that 21.15 kWh of heat was charged into the heat storage tank within 7.5 h, compared to 21.16 $\pm$ 0.85 kWh in the measurement. During discharge, 14.05 kWh of sensible heat was discharged as short term heat storage, and 7.65 kWh of latent heat can be released on demand as long term heat storage. The measured sensible and latent heat during discharge are 13.5 $\pm$ 0.54 kWh and 7.56 $\pm$ 0.30 kWh, respectively. The relative difference between the CFD calculated values is 1.2–3.7 %.

Further investigations are needed to optimize the flow pattern in the storage tank. For instance, the influence of the tube design on the heat transfer exchange capacity rate of the storage tank could be investigated, including tube diameter, length, tube number, layout, and the distance between tubes.

CRediT authorship contribution statement

Shan Chen: Research investigations, writing
Chang Yu: Reviewing, proof reading
Gang Wang: Providing measurement data
Weiqiang Kong: Reviewing
Zhiyong Tian: Reviewing
Jianhua Fan: Fund raising, idea formulation, editing.

Declaration of competing interest

The authors declare that they have no known competing financial interests or personal relationships that could have appeared to influence the work reported in this paper.

Data availability

Data will be made available on request.

Acknowledgments

The research is partly funded by the National Key Research and Development Program of China (No. 2021YFE0113500) and the Danish Energy Agency project for participation in joint IEA SHC Task 67 and ES Task 40 on "Compact Thermal Energy Storage; Materials within Components within Systems" (No. 134-21016). Without their support, the research would not be possible.

References

[1] D. Notz, A short history of climate change, in: EPJ Web of Conferences 246, 2020, pp. 1–11.
[2] C. Buchal, The challenge of discussing energy facts and climate change, in: EPJ Web of Conferences 246, 2020, pp. 1–12.
[3] P. Seljom, E. Rosenberg, A study of oil and natural gas resources and production, Int. J. Energy Sect. Manage. 5 (2011) 101–124.
[4] World Energy Council (WEC), World Energy Scenarios 2019 : Exploring Innovation Pathways to 2040, WEC publications, 2019.
[5] M. Roy, Solar as a sustainable energy, in: Idowu Samuel, R. Schmidpeter, Z.L. CN, A.R. DBM (Eds.), Encyclopedia of Sustainable Management [Internet], Springer International Publishing, Cham, 2020, pp. 1–6, https://doi.org/10.1007/978-3-030-02006-4_14-1. Available from.
[6] L. Luo, N. le Pierrès, Innovative Systems for Storage of thermal solar energy in buildings, in: Solar Energy Storage, 2015, pp. 27–62.
[7] Z. Zhou, Z. Zhang, J. Zuo, K. Huang, L. Zhang, Phase change materials for solar thermal energy storage in residential buildings in cold climate, Renew. Sust. Energ. Rev. 48 (2015) 692–703.
[8] Y. Tian, C.Y. Zhao, A review of solar collectors and thermal energy storage in solar thermal applications, Appl. Energy 104 (2013) 538–553.
[9] G. Drake, K. Harris, M. Heng, B. Appleby, L. Freiberg, P. Harding, et al., Development of a small-scale solar thermochemical energy storage system, in: GHTC 2017 - IEEE Global Humanitarian Technology Conference, Proceedings, 2017, pp. 1–8.
[10] G. Alva, L. Liu, X. Huang, G. Fang, Thermal energy storage materials and systems for solar energy applications, Renew. Sust. Energ. Rev. 68 (2017) 693–706.
[11] G. Alva, Y. Lin, G. Fang, An overview of thermal energy storage systems, Energy 144 (2018) 341–378.
[12] N. Delalić, R. Blažević, M. Alispahić, M. Torlak, A small-scale solar system with combined sensible- and latent-heat thermal energy storage, in: Lecture Notes in Networks and Systems, 2019, pp. 582–588.
[13] G. Englmair, M. Dannemand, S. Furbo, J. Fan, Combined short and long term heat storage with Sodium Acetate Trihydrate in cylindrical tanks, in: EuroSun 2018, Switzerland, 2018, pp. 1–3.
[14] H.W. Ryu, S.W. Woo, B.C. Shin, S.D. Kim, Prevention of supercooling and stabilization of inorganic salt hydrates as latent heat storage materials, Sol. Energy Mater. Sol. Cells 27 (2) (1992) 161–172.
[15] N. Xie, Z. Huang, Z. Luo, X. Gao, Y. Fang, Z. Zhang, Inorganic salt hydrate for thermal energy storage, Appl. Sci. (Switzerland) 7 (2017) 1–18.
[16] B.C. Zhao, R.Z. Wang, Perspectives for short-term thermal energy storage using salt hydrates for building heating, Energy 189 (2019) 1–6.
[17] A. Sharma, V.V. Tyagi, C.R. Chen, D. Buddhi, Review on thermal energy storage with phase change materials and applications, Renewable and Sustainable Energy Reviews 13 (2009) 318–345.
[18] Y. Tang, D. Gao, Y. Guo, S. Wang, T. Deng, Supercooling and phase separation of inorganic salt hydrates as PCMs, Appl. Mech. Mater. (2011) 2602–2605.
[19] M. Kubota, E.P. Ona, F. Watanabe, H. Matsuda, H. Hidaka, H. Kakiuchi, Studies on phase change characteristics of binary mixtures of erythritol and MgCl2·6H2O, J. Chem. Eng. Jpn. 40 (1) (2007) 80–84.
[20] R. Al-Shannaq, J. Kurdi, S. Al-Muhtaseb, M. Dickinson, M. Farid, Supercooling elimination of phase change materials (PCMs) microcapsules, Energy 87 (2015) 654–662.
[21] S. Furbo, Heat storage with an incongruently melting salt hydrate as storage medium based on the extra water principle, in: Thermal Storage of Solar Energy, Springer Netherlands, Dordrecht, 1981, pp. 135–145.
[22] L. Zhao, Y. Xing, X. Liu, Y. Luo, Thermal performance of sodium acetate trihydrate based composite phase change material for thermal energy storage, Appl. Therm. Eng. 143 (2018) 172–181.
[23] S.L. Hem, The effect of ultrasonic vibrations on crystallization processes, Ultrasonics 5 (4) (1967) 202–207.
[24] G. Wang, M. Dannemand, C. Xu, G. Englmair, S. Furbo, J. Fan, Thermal characteristics of a long-term heat storage unit with sodium acetate trihydrate, Appl. Therm. Eng. 187 (2021) 1–9.
[25] B. Sandnes, J. Rekstad, Supercooling salt hydrates: stored enthalpy as a function of temperature, Sol. Energy 80 (5) (2006) 616–625.
[26] G. Englmair, Y. Jiang, M. Dannemand, C. Moser, H. Schranzhofer, S. Furbo, et al., Crystallization by local cooling of supercooled sodium acetate trihydrate composites for long-term heat storage, Energy Build. 180 (2018) 159–171.
[27] M. Dannemand, W. Kong, J. Fan, J.B. Johansen, S. Furbo, Laboratory test of a prototype heat storage module based on stable supercooling of sodium acetate trihydrate, Energy Procedia (2015) 172–181.
[28] J. Fan, S. Furbo, E. Andersen, Z. Chen, B. Perers, M. Dannemand, Thermal behavior of a heat exchanger module for seasonal heat storage, Energy Procedia (2012) 244–254.
[29] Z. Ma, H. Bao, A.P. Roskilly, Study on solidification process of sodium acetate trihydrate for seasonal solar thermal energy storage, Sol. Energy Mater. Sol. Cells 172 (2017) 99–107.
[30] P. Tan, P. Lindberg, K. Eichler, P. Löveryd, P. Johansson, A.S. Kalagasidis, Effect of phase separation and supercooling on the storage capacity in a commercial latent heat thermal energy storage: experimental cycling of a salt hydrate PCM, J. Energy Storage 29 (2020) 1–20.
[31] W. Kong, M. Dannemand, J.B. Johansen, J. Fan, J. Dragsted, G. Englmair, et al., Experimental investigations on heat content of supercooled sodium acetate trihydrate by a simple heat loss method, Sol. Energy 139 (2016) 249–257.
[32] M. Dannemand, J. Dragsted, J. Fan, J.B. Johansen, W. Kong, S. Furbo, Experimental investigations on prototype heat storage units utilizing stable supercooling of sodium acetate trihydrate mixtures, Appl. Energy 169 (2016) 72–80.
[33] M. Dannemand, J.B. Johansen, W. Kong, S. Furbo, Experimental investigations on cylindrical latent heat storage units with sodium acetate trihydrate composites utilizing supercooling, Appl. Energy 177 (2016) 591–601.
[34] M. Dannemand, J.M. Schultz, J.B. Johansen, S. Furbo, Long term thermal energy storage with stable supercooled sodium acetate trihydrate, Appl. Therm. Eng. 91 (2015) 671–678.
[35] G. Englmair, C. Moser, S. Furbo, M. Dannemand, J. Fan, Design and functionality of a segmented heat-storage prototype utilizing stable supercooling of sodium acetate trihydrate in a solar heating system, Appl. Energy 221 (2018) 522–534.
[36] G. Wang, C. Xu, G. Englmair, W. Kong, J. Fan, S. Furbo, et al., Experimental and numerical study of a latent heat storage using sodium acetate trihydrate for short and long term applications, J. Energy Storage. 2022 (47) (November 2021), 103588.
[37] G. Verma, S. Singh, Computational multiphase iterative solution procedure for thermal performance investigation of phase change material embedded parallel flow solar air heater, J. Energy Storage 39 (2021) 1–18.
[38] T.D. Canonsburg, ANSYS Fluent Theory Guide 15317, ANSYS Inc, USA, 2013, 814 p.
[39] R.R. Kasibhatla, A. König-Haagen, D. Brüggemann, Numerical modelling of wetting phenomena during melting of PCM, Procedia Eng. 1 (157) (2016 Jan) 139–147.
[40] B.S. Negi, S. Singh, S. Negi, Multiphase numerical modeling of PCM integrated solar collector, in: Lecture Notes in Mechanical Engineering, 2021.
[41] S. Boskovic, B.V. Reddy, P. Basu, Encapsulated phase change materials for thermal energy storage: experiments and simulation, International Journal of Energy Research 26 (2) (2002) 159–171.
[42] M.H. Shojaeefard, G.R. Molaeimanesh, Y.S. Ranjbaran, Improving the performance of a passive battery thermal management system based on PCM using lateral fins, Waerme- Stoffuebertrag. (1995-) 55 (6) (2019) 1–15.
[43] M. Bechiri, K. Mansouri, Study of heat and fluid flow during melting of PCM inside vertical cylindrical tube, Int. J. Therm. Sci. 1 (135) (2019 Jan) 235–246.
[44] S.F. Hosseinizadeh, F.L. Tan, S.M. Moosania, Experimental and numerical studies on performance of PCM-based heat sink with different configurations of internal fins, Appl. Therm. Eng. (2011) 3827–3838.
[45] G. Zhou, Y. Han, Numerical simulation on thermal characteristics of supercooled salt hydrate PCM for energy storage: multiphase model, Appl. Therm. Eng. 125 (2017) 145–152.
[46] Ansys Fluent Customization Manual [Internet], Available from, 2022, http://www.ansys.com.
[47] G. Verma, S. Singh, S. Chander, P. Dhiman, Numerical investigation on transient thermal performance predictions of phase change material embedded solar air heater, J. Energy Storage 47 (2022).
[48] R. Li, Z. Liu, Y. Zhao, Y. Wu, J. Niu, L.Leon Wang, Fast fluid dynamics simulation of airflow around a single bluff body under different turbulence models and discretization schemes, Building and Environment 219 (2022), 109235. Jul 1.
[49] M. Mazzotti, T. Vetter, D.R. Ochsenbein, G.M. Maggioni, C. Lindenberg, Nucleation, in: Polymorphism in the Pharmaceutical Industry, Wiley-VCH Verlag GmbH & Co. KGaA, Weinheim, Germany, 2018, pp. 261–283.
[50] D. Turnbull, Phase changes, Solid State Phys. Adv. Res. Appl. 3 (C) (1956) 225–306.
[51] G. Englmair, S. Furbo, M. Dannemand, J. Fan, Experimental investigation of a tank-in-tank heat storage unit utilizing stable supercooling of sodium acetate trihydrate, Appl. Therm. Eng. 25 (167) (2020 Feb), 114709.